

SpikeDet: Better Firing Patterns for Accurate and Energy-Efficient Object Detection with Spiking Neural Networks

Yimeng Fan, Changsong Liu, Mingyang Li, Dongze Liu, Yanyan Liu[†], and Wei Zhang[†]

Abstract—Spiking Neural Networks (SNNs) are the third generation of neural networks. They have gained widespread attention in object detection due to their low power consumption and biological interpretability. However, existing SNN-based object detection methods suffer from local firing saturation, where adjacent neurons concurrently reach maximum firing rates, especially in object-centric regions. This abnormal neuron firing pattern reduces the feature discrimination capability and detection accuracy, while also increasing the firing rates that prevent SNNs from achieving their potential energy efficiency. To address this problem, we propose SpikeDet, a novel spiking object detector that optimizes firing patterns for accurate and energy-efficient detection. Specifically, we design a spiking backbone network, MDSNet, which effectively adjusts the membrane synaptic input distribution at each layer, achieving better neuron firing patterns during spiking feature extraction. For the neck, to better utilize and preserve these high-quality backbone features, we introduce the Spiking Multi-direction Fusion Module (SMFM), which realizes multi-direction fusion of spiking features, enhancing the multi-scale detection capability of the model. Furthermore, we propose the Local Firing Saturation Index (LFSI) to quantitatively measure local firing saturation. Experimental results validate the effectiveness of our method, with SpikeDet achieving superior performance. On the COCO 2017 dataset, it achieves 52.2% AP, outperforming previous SNN-based methods by 3.3% AP while requiring only half the power consumption. On object detection sub-tasks, including event-based GEN1, underwater URPC 2019, low-light ExDARK, and dense scene CrowdHuman datasets, SpikeDet also achieves the best performance.

Index Terms—Spiking Neural Network, Object Detection, Neuromorphic Computing, Energy-Efficient Detection.

I. INTRODUCTION

SPIKING Neural Networks (SNNs) have emerged as a promising alternative to traditional Artificial Neural Networks (ANNs) [1]. Unlike ANNs that rely on continuous values, spiking neurons in SNNs emulate biological neurons, computing and communicating through discrete spiking signals [2]. This spike-driven mechanism can avoid the computational burden of multiplication operations, instead relying on simpler addition operations, providing significant potential for energy-efficient computing [3]. Furthermore, the temporal

[†] Corresponding author: Yanyan Liu, Wei Zhang.

Yimeng Fan, Changsong Liu, Mingyang Li, Dongze Liu, and Wei Zhang are with the School of Microelectronics, Tianjin University, Tianjin 300072, China (e-mail: yimengfan@tju.edu.cn; changesong@tju.edu.cn; limingyang97@tju.edu.cn; ldz@tju.edu.cn; tjuzhangwei@tju.edu.cn).

Yanyan Liu is with the Optoelectronic Thin Film Device and Technology Research Institute, Nankai University, Tianjin 300350, China (e-mail: lyytianjin@nankai.edu.cn).

This work is supported by the Key Project of the Key Laboratory of Emergency Management for Fire Prevention and Control Technology in Industrial and Public Buildings in 2024 under Grant 2024KL0202.

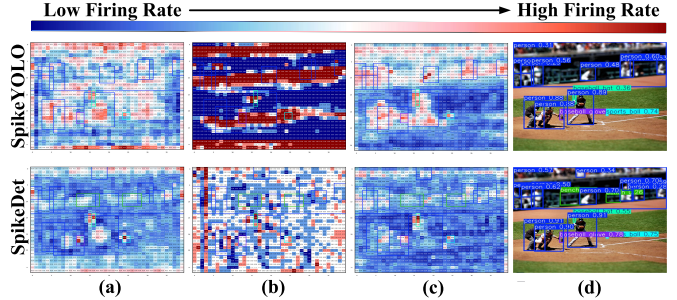


Fig. 1. **Visualization of local firing saturation problem in SNN-based object detector on COCO dataset.** Each pixel represents the neuron firing rate. (a) and (b) show feature maps before the detection head, as these features determine both classification and regression. (a) averages the 4D spike tensor ($[T, C, H, W]$) across both time and channel dimensions to show overall spatial firing distribution, while (b) selects a representative channel and averages across time steps to reveal individual neuron firing patterns. (c) shows neuron firing patterns of backbone features at 1/16 resolution. (d) presents the final detection results.

dynamics of these spikes provide SNNs with distinct representation capabilities [4]. Motivated by these characteristics, SNNs have been increasingly applied to various computer vision tasks [5]–[8].

Among these, SNNs have achieved competitive performance with ANNs on relatively simple tasks such as image classification [9], [10]. However, for more complex and widely applied tasks like object detection, which require simultaneous identification of object categories and precise prediction of their locations and sizes [11], [12], SNNs still face significant challenges. Specifically, performance gaps persist between SNN-based and ANN-based detectors [6], [10], [13]–[19]. More critically, the energy efficiency advantages of SNNs gradually diminish as their performance improves [10], [19].

These limitations motivate us to identify a fundamental problem in existing SNN-based detectors. As shown in Fig. 1, we observe that spiking neurons consistently reach maximum firing rates (firing saturation) in certain spatial regions, particularly in central regions of bounding boxes where object information is most concentrated [20], [21]. **We define this phenomenon, where multiple spatially adjacent neurons concurrently exhibit saturated firing patterns, as local firing saturation.** These saturated neurons are detrimental for SNN-based object detection. In SNNs, features are encoded through neuron firing patterns. When multiple adjacent neurons reach firing saturation, they produce identical representations, significantly reducing feature discriminability. This issue affects both components of object detection, consequently impacting detection accuracy. Specifically, for classification,

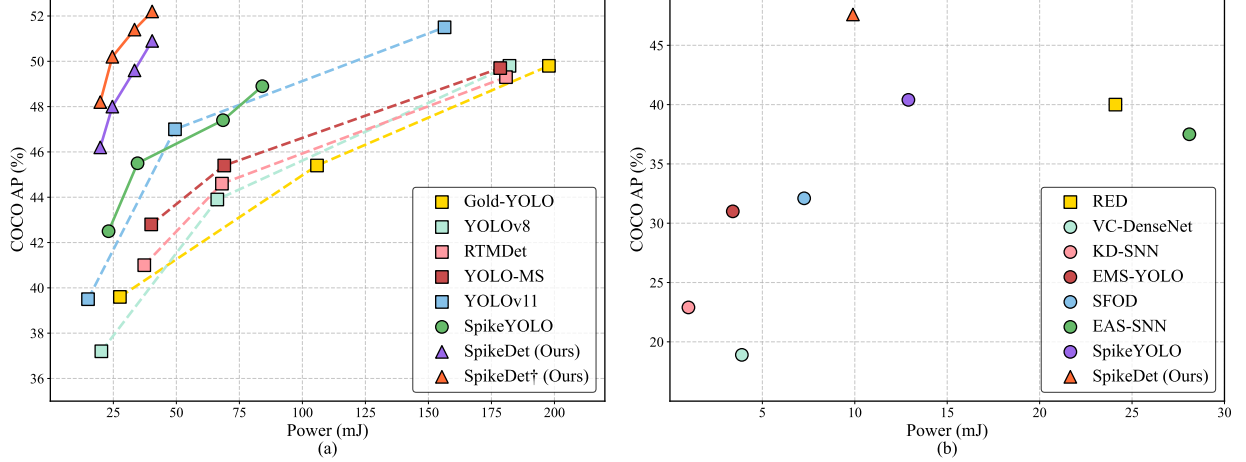


Fig. 2. Comparisons with other state-of-the-art methods on COCO AP and Power consumption. Squares represent ANN-based object detectors, circles represent SNN-based object detectors, and triangles represent our methods. (a) Comparison results on the COCO 2017 dataset. (b) Comparison results on the GEN1 dataset.

reduced feature discriminability causes multiple anchor points to produce similar confidence scores, preventing concentrated object representation and degrading overall confidence. For regression, this generates redundant bounding boxes that waste anchor resources and cause missed detections in overlapping scenes, such as the rear person and bench objects in Fig. 1 (d). Additionally, this local firing saturation issue increases the firing rate of SNN detectors, consequently raising their power consumption.

To address this issue, we propose SpikeDet, a novel spiking object detector. By optimizing neuron firing patterns, SpikeDet mitigates local firing saturation and achieves accurate, energy-efficient object detection. The core innovation of our approach is the introduction of a spiking backbone network, **Membrane-based Deformed Shortcut Residual Network (MDSNet)**. Current high-accuracy SNN object detectors [9], [10], [14], [19] employ membrane-based shortcuts [22] to achieve residual learning in their backbone networks for enhancing feature extraction capacity. However, this results in the residual path output being directly added to the shortcut path at each layer. As we theoretically analyze in Section IV-B1, such repeated path summation causes membrane synaptic input variance to accumulate across successive layers. This variance amplification significantly increases the probability of neurons receiving excessively large synaptic inputs. Consequently, neurons more frequently reach firing saturation. Combined with the inherently high neural activity in information-concentrated regions, this causes adjacent neurons to concurrently saturate, leading to the local firing saturation problem shown in Fig. 1(c). For this, we propose the Membrane-based Deformed Shortcut (MDS), which enables the identity mapping to stabilize its output distribution, fundamentally mitigating the local firing saturation problem. Based on MDS and residual architectures, we design MDSNet, which effectively combines the advantages of both, delivering powerful feature extraction capacity for SNN-based object detectors.

Multi-scale feature fusion also plays an important role in mitigating local firing saturation. For this, we propose the

Spiking Multi-direction Fusion Module (SMFM). In traditional spiking fusion methods [16], [19], information flows along limited paths. Such insufficient fusion raises two issues. First, features from different scales may simultaneously activate at object centers. Limited fusion prevents their effective integration, causing their responses to accumulate and leading to local firing saturation. Second, with limited fusion, shallow detail-sensitive features lack sufficient semantic modulation when integrated with deeper features, causing local firing saturation at regions with high local contrast in the fused representations. Multi-direction fusion creates multiple pathways, allowing features to undergo repeated refinement. This allows better integration of information across scales, mitigating local firing saturation while enhancing multi-scale feature utilization. Additionally, to quantitatively evaluate the capability of our method in addressing local firing saturation, we propose the Local Firing Saturation Index (LFSI). This metric averages the proportion of saturated neurons surrounding each neuron across all layers, reflecting the severity of local firing saturation in the network.

The main contributions of this work can be summarized as follows:

(1) We propose SpikeDet, an accurate and energy-efficient spiking object detector. The SpikeDet achieves better neuron firing patterns by optimizing the backbone and neck networks, thereby mitigating the local firing saturation problem faced by SNN-based object detectors.

(2) For the backbone, we propose MDSNet, which integrates MDS to regulate the membrane synaptic input distribution of subsequent neurons, enhancing firing pattern stability. For the neck, we design SMFM that implements multi-direction feature fusion in SNNs, preserving stable firing patterns while improving the model's multi-scale detection capability.

(3) Our method achieves superior performance, and its effectiveness in addressing local firing saturation is quantitatively verified by the proposed LFSI. On the COCO 2017 dataset [23] and various object detection sub-tasks, SpikeDet outperforms other SNN-based approaches while maintaining

the lowest power consumption.

The rest of this paper is organized as follows. In Section II, we report the related work. Then we provide the preliminaries of SNNs in Section III. Section IV introduces our proposed method. We present experiment results in Section V. Finally, we conclude this work in Section VI.

II. RELATED WORK

A. Spiking Neural Networks

SNNs are designed to mimic biological behavior more accurately than ANNs through spiking neurons [9]. However, the non-differentiable nature of neuron spike firing prevents SNNs from being trained with traditional backpropagation algorithms used in ANNs. To address this challenge, researchers have proposed two training approaches for SNNs: ANN2SNN conversion and direct training. The ANN2SNN conversion approach approximates ReLU activation using average firing rate, allowing trained ANNs to be transformed into SNNs [1]. Although this approach has led to powerful SNNs [13], it requires thousands of time steps. Moreover, this method is suited only for static datasets, and the performance of converted SNNs depends on the original ANNs. Conversely, the direct training method leverages surrogate gradients to optimize SNNs [16], facilitating their training on a variety of datasets and achieving strong performance within a limited number of time steps. Therefore, we employ the direct training strategy in this study.

To advance the performance of SNNs and realize deeper architectures, researchers have proposed numerous SNN-based residual learning methods [22], [24], [25]. Among them, SEW-ResNet [25] and MS-ResNet [22] address gradient issues and train networks exceeding 100 layers. However, the former does not consider the non-spiking convolutions caused by spike addition. The latter solves this issue but introduces a local firing saturation problem that we identify in this work. This paper further investigates SNN characteristics to enhance feature extraction while maintaining a full-spiking network.

B. Object Detection

Object detection is an important and highly complex task in computer vision. Early object detection methods relied on hand-crafted features and sliding window approaches, achieving good accuracy in face detection [26]. With the development of Artificial Neural Networks (ANNs) [27], [28], ANN-based methods gradually became mainstream. These can be categorized into two-stage and one-stage object detectors. Two-stage methods consist of a proposal generator and a region-wise prediction subnetwork [29]. Although they can achieve good performance, they have gradually been replaced by one-stage methods due to their complex design and inefficient inference. One-stage methods directly generate object locations and classifications, significantly reducing computational complexity while maintaining competitive accuracy. Representative examples include YOLO [30]–[32] and DETR [33] series.

C. Object Detection with Spiking Neural Networks

Early attempts to apply SNNs to object detection using ANN2SNN conversion [13], [34] face the challenges of high latency, poor performance, and incompatibility with event cameras. VC-DenseNet [6] and EMS-YOLO [14] pioneer direct training for SNN-based object detection, achieving promising results on both static and event-based datasets. SFOD [16] first introduces an efficient Spiking Fusion Module for SNNs. SpikeYOLO [19] proposes the I-LIF neuron to address the impact of quantization errors from spiking neurons on object detection, significantly improving the performance of SNN-based detectors. However, both approaches overlook the fundamental differences between SNN-based and ANN-based feature representations, i.e., SNN features are represented through neuron firing patterns. This oversight amplifies their performance gap with ANN-based detectors. Hence, our research enhances the SNN object detector by improving neuron firing patterns.

III. THE PRELIMINARIES OF SNNs

A. Spiking Neurons

To achieve a balance between biological plausibility and computation complexity in SNNs, researchers have introduced various spiking neural models, including the Hodgkin-Huxley [35], Integrate-and-Fire (IF) [36], Leaky Integrate-and-Fire (LIF) [37], and Integer Leaky Integrate-and-Fire (I-LIF) [19] models, among others. In our work, we employ the I-LIF neuron due to its effectiveness in reducing the quantization error problem of SNNs. The I-LIF neuron model is represented by:

$$\mathbf{u}^{t,n} = \tau \mathbf{h}^{t-1,n} + \mathbf{x}^{t,n}, \quad (1)$$

$$\mathbf{o}^{t,n} = \text{Clip}(\text{round}(\mathbf{u}^{t,n}), 0, D), \quad (2)$$

$$\mathbf{h}^{t,n} = \mathbf{u}^{t,n} - V_{th} \cdot \mathbf{o}^{t,n}. \quad (3)$$

Here, \mathbf{u} represents the membrane potential, \mathbf{h} the membrane potential retained from the previous time step, \mathbf{x} the pre-synaptic input, and \mathbf{o} the output spike. Variables t and n denote time step and layer number, respectively. Function $\text{Clip}(x, \min, \max)$ constrains x within $[\min, \max]$, while $\text{round}(x)$ rounds x to the nearest integer. D is the upper limit hyperparameter for integer-valued spike activation, τ is the membrane potential decay constant, and V_{th} is the membrane potential threshold. The core of the I-LIF neuron lies in Eq. 2, which enables neurons to generate integer spikes during training and can convert them to the sum of binary spikes in D time steps of Soft-Reset IF neurons during inference [10].

B. Surrogate Gradient Training Strategy

In SNN training, a key challenge arises from the non-differentiable nature of the spike generation process described in Eq. 2. To overcome this limitation and enable effective back-propagation within contemporary deep learning frameworks, we implement surrogate gradient techniques. The surrogate gradient applied to Eq. 2 is expressed as:

$$\frac{\partial \mathbf{s}^{t,n}}{\partial \mathbf{u}^{t,n}} = \begin{cases} 1, & \text{if } 0 \leq \mathbf{u}^{t,n} \leq D \\ 0, & \text{otherwise.} \end{cases} \quad (4)$$

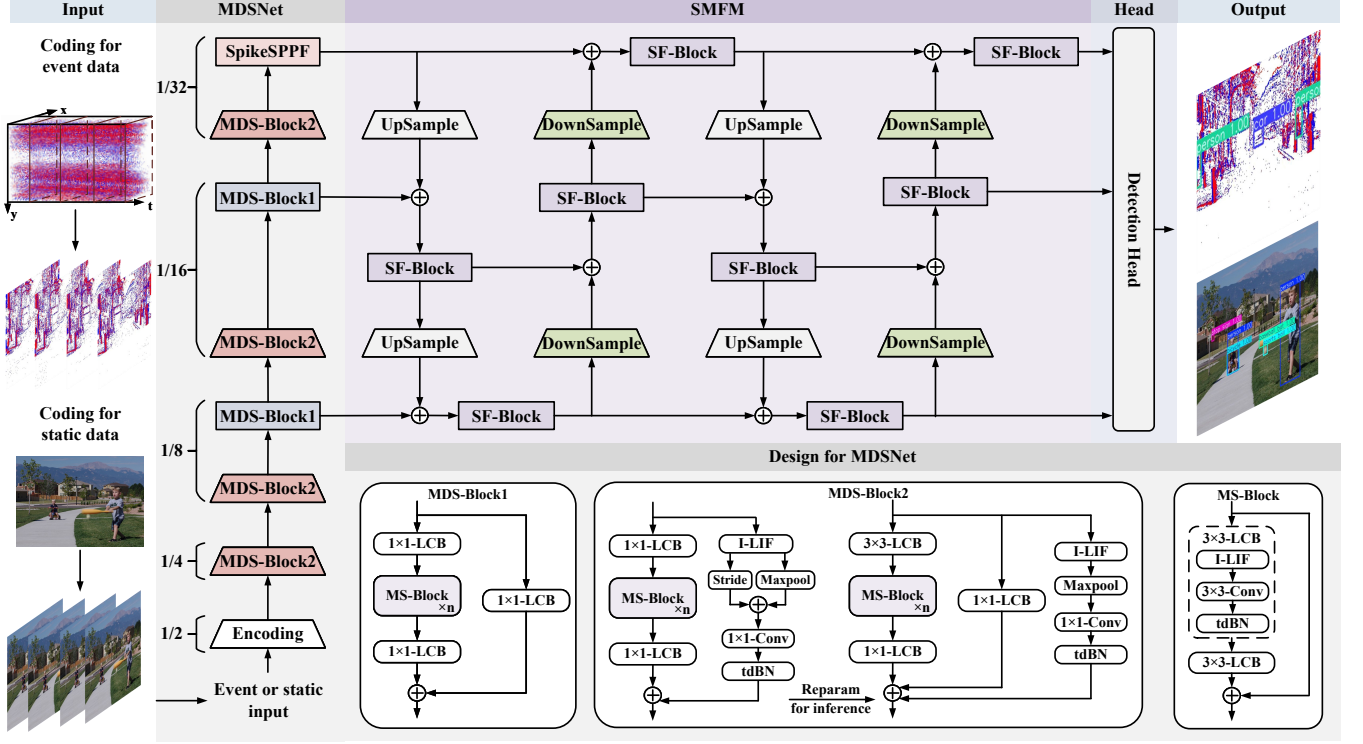


Fig. 3. **The architecture of SpikeDet.** SpikeDet comprises MDSNet, SMFM, and the SpikeYOLO Detection Head [19]. The model receives two types of inputs: event and static data, with the input coding and output represented in the figure. The core of SpikeDet is MDSNet, which consists of 5 stages. Each stage downsampling factor relative to the original input is marked in the figure, with MDS-Block1 and MDS-Block2 performing feature extraction without and with downsampling, respectively. By incorporating MDS, this architecture successfully stabilizes the firing patterns at each stage, alleviating the local firing saturation problem. Additionally, SMFM enables multi-direction feature fusion, allowing features to undergo multiple refinements through the model, thereby improving the model’s capability to detect multi-scale objects and preserving neuron firing patterns.

For common LIF neurons, the spike firing formula is

$$\mathbf{o}^{t,n} = \text{Hea}(\mathbf{u}^{t,n} - V_{th}). \quad (5)$$

The corresponding surrogate gradient is expressed as:

$$\frac{\partial \mathbf{o}^{t,n}}{\partial \mathbf{u}^{t,n}} = \frac{1}{a} \text{sign}\left(|\mathbf{u}^{t,n} - V_{th}| \leq \frac{a}{2}\right), \quad (6)$$

with a serving as a normalization coefficient that guarantees the function integrates to 1.

IV. METHODOLOGY

A. Overview

The architecture of our proposed SpikeDet is shown in Fig. 3. As illustrated, the model adopts the backbone-neck-head architecture widely used in object detection frameworks [16], [30], [32], [38], [39]. For the backbone, we propose MDSNet to extract multi-scale features with more stable firing patterns. For the neck, we design a Spiking Multi-direction Fusion Module (SMFM), which enables the model to enhance backbone features through multi-direction fusion. For the detection head, which primarily generates detection results from formed features, establishing firing pattern stability is not critical. Therefore, we directly adopt the existing SpikeYOLO Detection Head [19].

The spike-driven characteristics of SNNs make them naturally suitable for event data. Consequently, SNN-based detectors are now being explored on not only traditional static

datasets but also event-based datasets. To handle both types of data effectively and fully exploit the temporal dynamics of SNNs, we encode the inputs as 4D tensors $[T, C, H, W]$, where T represents time steps, C denotes the number of channels, while H and W correspond to spatial dimensions. For static data, we employ the direct coding method [40], replicating the input T times to form a time train that supports the temporal processing requirements of the model. For event data, event cameras can asynchronously collect millions of events per second. Each event is defined as $e_k = (t_k, p_k, x_k, y_k)$, where x_k and y_k are spatial coordinates, t_k is the timestamp, and p_k represents polarity. Therefore, to effectively reduce data volume while preserving sparse characteristics, we adopt the coding approach from [19], [22]. This approach first selects a specific time window, divides it into T temporal bins, and integrates events within each bin into frame format, thereby forming the aforementioned 4D tensor representation. Finally, we use Rate Decoding [16] for model output decoding, followed by Non-Maximum Suppression (NMS) post-processing.

B. MDSNet

1) *Motivation:* Object detection is a complex task that demands strong feature extraction capabilities from the backbone network. In SNNs, to address this requirement, extensive studies have been conducted on SNN-friendly residual learning approaches [22], [24], [25], as constructing deep networks

through residual learning has been proven beneficial in ANNs. Among these efforts, MS-ResNet [22] is the most successful approach, featuring its membrane-based shortcut. This design enables efficient information propagation in deep SNN-based models. Building upon this, subsequent backbones such as EMS-ResNet [14] and S-Backbone [19] have been proposed, enabling the development of advanced SNN-based object detectors. Taking EMS-ResNet as an example, this network can be described as follows,

$$\psi = \text{tdBN} \circ \text{Conv} \circ \text{SN}, \quad (7)$$

$$\mathbf{y}_I^{t,l} = \psi(\psi(\mathbf{x}^{t,l})) + \mathbf{x}^{t,l}, \quad (8)$$

$$\mathbf{y}_{D1}^{t,l} = \psi(\psi(\mathbf{x}^{t,l})) + \text{Cat}[\text{MPool}(\mathbf{x}^{t,l}), \psi(\text{MPool}(\mathbf{x}^{t,l}))], \quad (9)$$

$$\mathbf{y}_{D2}^{t,l} = \psi(\psi(\mathbf{x}^{t,l})) + \psi(\text{MPool}(\mathbf{x}^{t,l})). \quad (10)$$

Here, \mathbf{y} represents the output and \mathbf{x} represents the input. tdBn, Conv, SN, MPool, and Cat denote threshold-dependent Batch Normalization [24], convolution, I-LIF neurons, Maxpool, and channel dimension concatenation, respectively. ψ denotes I-LIF-Conv-tdBN (LCB). The superscript l denotes the l -th residual block, while subscripts D and I indicate whether the residual block performs downsampling or not. Accordingly, Eq. 8 represents the MS-Block without downsampling, while Eqs. 9 and 10 represent the downsampling blocks EMS-Block1 and EMS-Block2, respectively.

When the model goes deeper, MS-Blocks are stacked repeatedly. For ease, let $\mathbf{y}_R^{t,l}$ and $\mathbf{y}_S^{t,l}$ denote the residual and shortcut path outputs, with variances $\text{Var}[\mathbf{y}_R^{t,l}]$ and $\text{Var}[\mathbf{y}_S^{t,l}]$, respectively. For the output variance of the MS-Block $\text{Var}[\mathbf{y}_I^{t,l}] = \text{Var}[\mathbf{y}_R^{t,l} + \mathbf{y}_S^{t,l}]$, we have

$$\text{Var}[\mathbf{y}_I^{t,l}] = \text{Var}[\mathbf{y}_R^{t,l}] + 2\text{Cov}[\mathbf{y}_R^{t,l}, \mathbf{y}_S^{t,l}] + \text{Var}[\mathbf{y}_S^{t,l}]. \quad (11)$$

To further analyze this, we derive the following proposition. This property holds under standard initialization schemes [41]. It continues to hold approximately during and after training due to weight decay and the stabilizing effect of tdBn.

Proposition 1. *For d stacked LCB layers ($d \geq 1$) with arbitrary kernel sizes, under the convolution zero-mean weight and zero bias initialization, the output at the $(n+d)$ -th layer $\mathbf{y}^{t,n+d}$ is uncorrelated with the input at the n -th layer $\mathbf{x}^{t,n}$.*

Proof The detailed proof is presented in Appendix A-A.

Based on Proposition 1, the residual path $\mathbf{y}_R^{t,l} = \psi(\psi(\mathbf{x}^{t,l}))$ is the output of 2 stacked LCB layers processing the input $\mathbf{x}^{t,l}$, while the shortcut path $\mathbf{y}_S^{t,l} = \mathbf{x}^{t,l}$. Therefore, we have $\text{Cov}[\mathbf{y}_R^{t,l}, \mathbf{y}_S^{t,l}] = 0$. Thus $\text{Var}[\mathbf{y}_I^{t,l}] = \text{Var}[\mathbf{y}_R^{t,l}] + \text{Var}[\mathbf{y}_S^{t,l}]$. For k stacked MS-Blocks, we can recursively derive that

$$\text{Var}[\mathbf{y}_I^{t,k}] = \text{Var}[\mathbf{y}_S^{t,1}] + \sum_{l=1}^k \text{Var}[\mathbf{y}_R^{t,l}]. \quad (12)$$

Therefore, the variance of $\mathbf{y}_I^{t,l}$ becomes increasingly large as the network deepens. This results in unstable membrane synaptic input distribution in subsequent neurons.

Proposition 2. *For I-LIF neurons, the variance of the membrane potential is proportional to the variance of the input, i.e., $\text{Var}[\mathbf{u}^{t,n}] \propto \text{Var}[\mathbf{x}^{t,n}]$.*

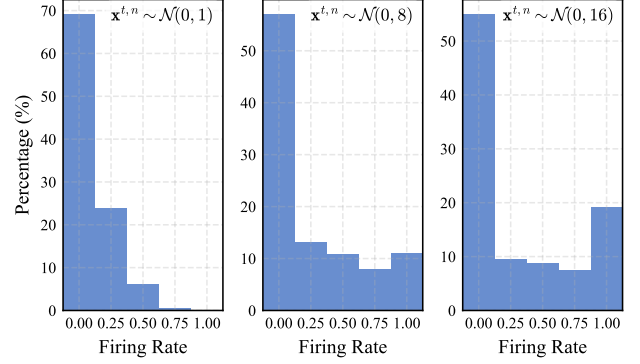


Fig. 4. **Firing rate distribution of I-LIF neurons for different presynaptic input $\mathbf{x}^{t,n}$ when $T = 1$ and $D = 4$.** The input \mathbf{x} is sampled from Gaussian distributions with different variances. Increased variance leads to higher firing saturation probability.

Proof The detailed proof is presented in Appendix A-B.

With Proposition 2, we can conclude that the aforementioned variance accumulation in synaptic input directly creates unstable membrane potential distributions. According to Eq. 2, this instability increases the probability of neurons firing large integer-valued spikes, thereby exacerbating the local firing saturation problem. This severely impacts object detection tasks as discussed in Section I. Fig. 4 confirms our analysis, visually demonstrating that unstable input leads to more active neuron firing patterns. Additionally, as shown in Eqs. 9 and 10, during downsampling, the model positions Maxpool operations before I-LIF neurons. Since Maxpool selects maximum values from local regions, it increases the input intensity received by I-LIF neurons. This raises the risk of local firing saturation.

2) MDSNet Architecture: To address these issues, as shown in Fig. 3, we propose MDSNet, a novel SNN-based ResNet-like backbone network. On the shortcut path, we propose a Membrane-based Deformed Shortcut (MDS), which incorporates 1×1 -LCB, i.e., LCB using 1×1 convolution. This structure converts input to spikes through the I-LIF layer and processes them through a 1×1 convolution, which improves expressiveness capability. The tdBn component further provides this path with the ability to adjust the output distribution. This fundamentally addresses the variance accumulation problem in Eq. 12, which is also experimentally verified in Section V-C1. On the residual path, we place MS-Blocks in it rather than on the main path. It provides a clean gradient propagation path for deep networks. Additionally, to avoid the aforementioned problems with stacked MS-Blocks, we place a 1×1 -LCB at both the input and output to control variance. Through improvements on both paths, we ensure the output distribution stability of each block in MDSNet. Meanwhile, structural enhancements preserve the efficient information propagation advantage offered by the membrane-based shortcut in deep networks.

Specifically, MDSNet consists of MDS-Block1 and MDS-Block2. MDS-Block1 is designed without downsampling, following the structure described above. MDS-Block2 serves as the downsampling block. Its residual path is identical to MDS-Block1. In the shortcut path, however, we position

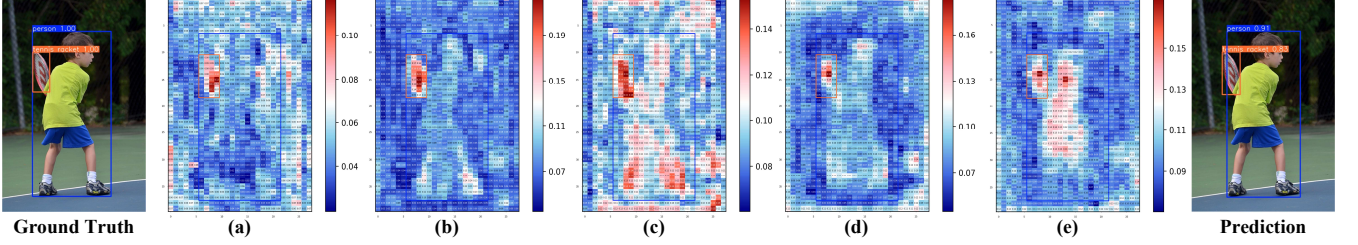


Fig. 5. **Influence of multi-direction feature fusion on firing patterns of SNN-based detector.** We visualize feature maps at the 1/16 downsampling stage, averaging across T and C dimensions to reveal overall firing patterns. Figures (a) to (e) show neuron firing patterns for feature maps with no fusion, one-way, two-way, three-way, and four-way fusion, respectively.

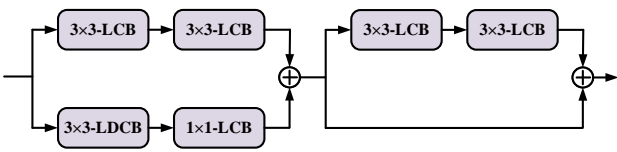


Fig. 6. **The architecture of the proposed SF-Block.** The difference between 3x3-LDCB and 3x3-LCB lies in that the former replaces the 3x3 convolution with a 3x3 depthwise convolution.

Maxpool after the I-LIF layer to avoid the amplified input to I-LIF. Additionally, to better preserve balanced information during downsampling, we also employ fixed stride downsampling. After downsampling, the stride and Maxpool results are weighted, added, convolved, and followed by tdBn for distribution adjustment. To eliminate non-spiking computations caused by pre-convolution addition during inference, we reparameterize this structure by splitting the shortcut path. One path combines fixed stride downsampling with 1x1 convolution to form a 1x1-LCB path, while the other integrates Maxpool after the I-LIF layer in 1x1-LCB.

C. Analysis of Gradient Vanishing/Explosion for MDSNet

To demonstrate that the MDS does not affect the training and convergence, we use the Block Dynamical Isometry [42] to verify that MDSNet can effectively overcome the gradient vanishing or explosion problem.

Consider a serial network as shown in Eq. 13, where f_j represents the j -th layer of the network. The Jacobian matrix from input to output of the j -th layer can be denoted as $J_j = \frac{\partial f_j}{\partial f_{j-1}}$. Furthermore, let $\phi(J)$ be defined as the expectation of $\text{tr}(J)$, while $\varphi(J) = \phi(J^2) - \phi^2(J)$

$$f(x) = f_L \circ f_{L-1} \circ \dots \circ f_1(x) \quad (13)$$

Definition 1. (Definition 3.1. in [42]) Consider a neural network that can be represented as a series of blocks as Eq. 13 and the j -th block's Jacobian matrix is denoted as J_j . If $\forall j$, $\phi(J_j J_j^T) \approx 1$ and $\varphi(J_j J_j^T) \approx 0$, the network achieves Block Dynamical Isometry and can avoid gradient vanishing or explosion.

Definition 2. (Definition 5.1. in [42]) Let $f(x)$ be a transform whose Jacobian matrix is J . f is called general linear transform when it satisfies:

$$E \left[\frac{\|f(x)\|_2^2}{\text{len}(f(x))} \right] = \phi(J J^T) E \left[\frac{\|x\|_2^2}{\text{len}(x)} \right]. \quad (14)$$

Theorem 1. (Theorem 4.1. in [42]) Given $J := \prod_{j=L}^1 J_j$, where $\{J_j \in \mathbb{R}^{m_j \times m_{j-1}}\}$ is a series of independent random matrices. If $(\prod_{j=L}^1 J_j)(\prod_{j=L}^1 J_j)^T$ is at least the 1st moment unitarily invariant, we have

$$\phi \left(\left(\prod_{j=L}^1 J_j \right) \left(\prod_{j=L}^1 J_j \right)^T \right) = \prod_{j=L}^1 \phi(J_j J_j^T). \quad (15)$$

Since the information transmitted in the network can be considered as random variables [43], $E \left[\frac{\|x\|_2^2}{\text{len}(x)} \right]$ is regarded as the second-order moment of the input, denoted by α_2 . Building on the derivations in [14], [24], [42] and Definitions 1 and 2, we can independently analyze each MDS-Block. Subsequently, by applying Theorem 1 to these individual analyses, we can derive the overall behavior of the MDSNet.

Proposition 3. For MDSNet, when the encoding layer output follows $x^t \sim \mathcal{N}(0, 1)$ and each block output follows $x^{t,j} \sim \mathcal{N}(0, 1)$, the network satisfies: $\phi(J J^T) \approx 1$.

Proof. The details can be found in Appendix A-C.

As elucidated in [14], [22], in the majority of cases, $\phi(J J^T) \approx 1$ is sufficient to guarantee that the network avoids gradient vanishing or explosion. The condition $\varphi(J_j J_j^T) \approx 0$ is imposed to preclude the occurrence of accidental situations. Therefore, Proposition 3 provides theoretical support for the ability of MDSNet to address the problem of gradient vanishing or explosion.

D. SMFM

Research in feature fusion for SNNs is limited to one-way and two-way fusion [16], [19], where large-scale and small-scale features are combined only a limited number of times. As discussed in Section I, such insufficient fusion leads to local firing saturation in both object centers and regions with high local contrast. This makes multi-directional feature fusion more critical in SNNs than in ANNs. To address these issues, we propose the Spiking Multi-directional Fusion Module (SMFM). It enables the model to repeatedly integrate multi-scale features through iterative fusion, allowing more

comprehensive feature fusion. Fig. 5 provides visualization evidence that multi-direction fusion effectively mitigates local firing saturation.

The structure of the SMFM is shown in Fig. 3. In this module, feature maps ranging from 1/8 to 1/32 are fused. During the fusion process, we first fuse feature maps of lower resolution with those of higher resolution through upsampling. Following this, we employ downsampling to further integrate these fused feature maps. This process is then repeated iteratively. Next, we will discuss the methods for upsampling, downsampling, and spiking feature fusion.

To achieve upsampling/downsampling, we use Nearest-Neighbor Interpolation (NNI) with 1×1 -LCB and 3×3 -LCB with a stride of 2 as core elements. For feature fusion, we multiply the feature maps by learnable constants and then add them together. These constants can be fused with the previous tDBN layer. As the features serve as presynaptic inputs to neurons, this method is compatible with SNNs. In this way, we achieve better feature alignment through adaptive weighting of different-scale features without extra parameters. Then, as shown in Fig. 6, we propose the Spiking Fusion Block (SF-Block) to enhance the fused features. This block consists of two sub-blocks. The first has two paths, with one containing two stacked 3×3 -LCBs and another containing a 3×3 -LDCB (with internal depthwise convolution) followed by a 1×1 -LCB, which enables feature extraction from different receptive fields. The second is an MS-Block for residual learning that further adjusts these features.

V. EXPERIMENT

A. Experimental Setup

1) *Implementation Details*: For I-LIF neurons, the membrane time constant τ is initialized to 0.25. The models are trained on 4 NVIDIA A6000 GPUs, using the SGD optimizer with a learning rate of 0.01. During post-processing, we use NMS, and the top 100 boxes are selected for evaluation. Additionally, we use Complete IoU (CIOU) [44] and Distribution Focal Loss (DFL) [45] for bounding box regression, and Binary Cross Entropy (BCE) [46] for classification loss. For multiscale evaluation, following [47], we employ both original and horizontally flipped images at scale factors of 0.6, 1.0, 1.2, 1.5, and 1.8.

2) *Datasets*: The COCO 2017 is a large-scale object detection benchmark with 118,287 training and 5000 validation images, which we use for training and testing, respectively [23]. Objects from 80 categories are annotated with their classes and locations. On this dataset, we train for 400 epochs with a batch size of 64 at a resolution of 640×640 , employing mosaic [48] and mixup [49] data augmentation during training.

3) *Benchmark Settings: Average Precision*. Following [31], [38], [47], [48], we report Average Precision (AP) as the primary metric. We also evaluate AP at IoU thresholds of 0.5 and 0.75, as well as AP for small, medium, and large objects.

Firing Rate. The firing rate, which measures neuronal activity, is another critical metric for evaluating SNNs. It is calculated as the average ratio of neuron spikes to the total number of neurons across all time steps.

FLOPs and SOPs. We also evaluate the computational cost of ANNs and SNNs. For ANNs, we use FLOPs (Floating-point OPerations, including additions and multiplications) as the metric. The FLOPs are calculated as:

$$\text{FLOPs} = \sum_{n=1}^N 2 \times C^{n-1} \times C^n \times (K^n)^2 \times H^n \times W^n, \quad (16)$$

where n denotes the layer index, N denotes the total number of layers, K denotes the kernel size, and C, H, W represent the channel number and spatial dimensions as previously defined. For SNNs, FLOPs is not a suitable metric for computational cost as their computation relies on sparse spike operations without multiplications. Therefore, we employ SOPs (Synaptic OPerations) as the metric, which is calculated as:

$$\text{SOPs} = \sum_{t=1}^T \sum_{n=1}^N fr^{t,n-1} \times C^{n-1} \times C^n \times (K^n)^2 \times H^n \times W^n, \quad (17)$$

where t denotes the time step, T denotes the total number of time steps, and fr denotes the firing rate.

Theoretical Energy Evaluation. Our energy evaluation adopts the standard approach in the SNN field [9], [10], [19], which employs theoretical computational metrics independent of specific hardware platforms. This theoretical estimation merely serves to facilitate qualitative energy comparisons among different SNN and ANN algorithms. For SNNs, the power consumption is computed as $E_{\text{SNNs}} = E_{\text{AC}} \times \text{ACs}$, where ACs denotes the number of accumulation calculations. Since SOPs consist entirely of accumulation operations, we have $\text{ACs} = \text{SOPs}$. For ANNs, the power consumption is computed as $E_{\text{ANNS}} = E_{\text{MAC}} \times \text{MACs}$, where MACs denotes the number of multiply-accumulate operations, and $\text{FLOPs} = 2 \times \text{MACs}$. Additionally, following previous works, we adopt $E_{\text{AC}} = 0.9 \text{ pJ}$ and $E_{\text{MAC}} = 4.6 \text{ pJ}$ as the power consumption for a single AC and MAC operation, respectively.

B. Local Firing Saturation Index

1) *Definition*: To quantify the effectiveness of our method in addressing the local firing saturation problem, we define a Local Firing Saturation Index (LFSI). For the n -th layer with spike feature map $\mathbf{O} \in \mathbb{R}^{T \times C^n \times H^n \times W^n}$, a neuron at (c, h, w) is **saturated** if it fires at maximum rate:

$$\mathbb{I}_{\text{sat}}(\mathbf{O}^{c,h,w}) = \begin{cases} 1, & \text{if } \sum_{t=1}^T \mathbf{O}^{t,c,h,w} = T \times D \\ 0, & \text{otherwise.} \end{cases} \quad (18)$$

For each neuron at location (c, i, j) , we compute its local firing saturation density over a $S \times S$ spatial neighborhood $\mathcal{W}_{i,j}$ within channel c ,

$$\rho(c, i, j) = \frac{1}{S^2} \sum_{(p,q) \in \mathcal{W}_{i,j}} \mathbb{I}_{\text{sat}}(\mathbf{O}^{c,p,q}). \quad (19)$$

The LFSI for a single layer is the average across all channels and spatial locations,

$$\text{LFSI}^n = \frac{1}{C^n H^n W^n} \sum_{c=1}^{C^n} \sum_{i=1}^{H^n} \sum_{j=1}^{W^n} \rho(c, i, j). \quad (20)$$

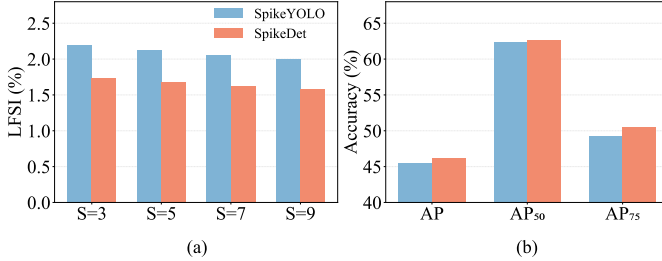


Fig. 7. (a) LFSI comparison between SpikeDet and SpikeYOLO across different spatial neighborhood sizes S . (b) AP comparison at different IoU thresholds.

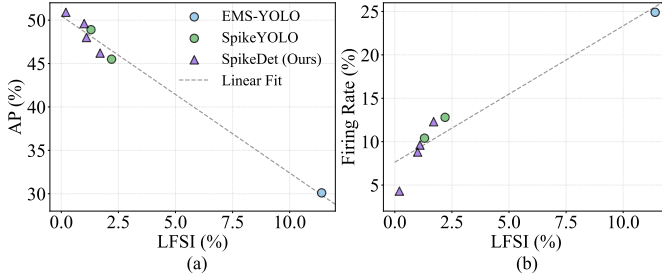


Fig. 8. Correlation analysis of LFSI across different SNN-based object detectors. (a) Correlation between LFSI and detection performance. (b) Correlation between LFSI and firing rate.

For a network with N spiking layers, the overall LFSI is

$$\text{LFSI} = \frac{1}{N} \sum_{n=1}^N \text{LFSI}^n. \quad (21)$$

A higher LFSI indicates more severe local firing saturation, with $\text{LFSI} \in [0, 1]$.

2) *Analysis of LFSI Under Varying Spatial Neighborhoods:* The parameter S critically affects LFSI evaluation strictness. Small S requires saturated neurons to be spatially contiguous, while large S allows them to be separated within the neighborhood. To investigate this relationship, we analyze LFSI values across different S settings. We conduct experiments on SpikeYOLO [19] and the proposed SpikeDet models to observe the general behavior of this metric. As shown in Fig. 7, the LFSI values of both methods decrease as S increases, confirming the expected relaxation in evaluation criteria. Notably, our method consistently outperforms SpikeYOLO in terms of LFSI across all S values, demonstrating superior capability in mitigating local firing saturation. Moreover, our approach achieves a higher AP across all IoU thresholds, further validating the importance of addressing the local firing saturation problem. Based on these observations, we adopt $S = 3$ for subsequent experiments as it provides the most stringent assessment of local firing saturation.

3) *Correlation Analysis of LFSI:* To further validate the importance of addressing local firing saturation, we analyze the correlation between LFSI and detection performance across different model variants, including SpikeDet, SpikeYOLO, and EMS-YOLO. As illustrated in Fig. 8 (a), LFSI exhibits a strong negative correlation with AP (Pearson $r = -0.992$, $p < 0.001$), demonstrating that mitigating local firing satu-

TABLE I
THE ABLATION STUDY ON MDSNET. THE SPECIFIC CONFIGURATION OF THE PROPOSED MDSNET IS DETAILED IN APPENDIX B. MS AND PLAIN INDICATE MDSNET WITH MDS REPLACED BY MEMBRANE-BASED SHORTCUTS AND REMOVED, RESPECTIVELY.

Backbone	Depth	AP	AP ₅₀	Param (M)	Firing Rate(%)	LFSI (%)	Power (mJ)
EMS-ResNet [14]	34	43.2	59.5	22.9	14.6	3.2	22.7
SEW-ResNet [25]	34	43.2	59.7	22.9	12.2	1.6	51.1
MS-ResNet [22]	34	43.8	60.5	22.9	12.2	1.7	21.3
S-Backbone [19]	47	44.0	60.6	24.2	12.2	1.7	30.4
MDSNet	34	44.8	61.2	22.0	11.8	1.5	19.0
MDSNet-MS	34	44.2	60.6	21.9	12.0	1.6	19.3
MDSNet-Plain	34	43.7	60.5	21.9	11.4	1.4	18.3
MDSNet	10	41.5	58.2	14.3	12.9	1.9	16.2
MDSNet	18	43.1	59.5	17.5	12.4	1.8	17.5
MDSNet	104	46.5	63.2	48.2	9.1	0.9	23.3

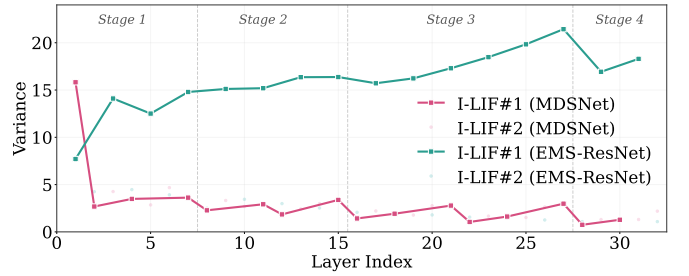


Fig. 9. Presynaptic input variance across layers. Experiments are conducted using MDSNet34 and EMS-ResNet34 on COCO. The backbone is divided into 4 stages based on feature map sizes, where I-LIF#1 and I-LIF#2 denote the first and second neurons in the residual path, respectively.

ration is crucial for improving SNN-based object detection. Detailed configurations of SpikeDet variants are provided in Section V-D. Additionally, Fig. 8 (b) reveals a strong positive correlation between LFSI and firing rate (Pearson $r = 0.955$, $p < 0.001$). Since firing rate directly determines energy consumption as shown in Eq. 17, mitigating local firing saturation effectively reduces power consumption.

C. Ablation Studies

In this section, we demonstrate the effectiveness of MDSNet through backbone network comparisons and investigate how model depth, SMFM, SF-Block, and time step affect performance. For efficiency, ablation studies are conducted with 150 epochs, ensuring convergence for reliable comparison.

1) *The Effectiveness of MDSNet:* To demonstrate the feature extraction capabilities of MDSNet, we compare it with the most advanced SNN backbones available. For fair comparison, we construct models using the backbone networks paired with identical neck and detection head architectures. The comparison results are shown in rows 1 to 5 of Table I. These results demonstrate that MDSNet34 significantly outperforms other models in AP and AP₅₀, while achieving lower LFSI, firing rate, and power consumption. Additionally, we conduct comparative experiments by replacing MDS with membrane-based shortcuts and removing MDS. As shown in rows 5 to 7 of Table I, replacing MDS with membrane-based shortcuts increases LFSI, firing rate, and power consumption while reducing AP, demonstrating the effectiveness of MDS

TABLE II
EFFECTIVENESS OF SMFM.

Fusion Method	Fusion Directions	AP	AP ₅₀	Param (M)	Firing Rate(%)	LFSI (%)	Power (mJ)
SMFM	1	41.3	58.6	21.1	13.1	1.7	19.5
SMFM	2	43.0	59.9	21.6	12.2	1.6	17.6
SMFM	4	44.8	61.2	22.0	11.8	1.5	19.0
SMFM	6	44.2	60.7	22.1	11.3	1.3	19.6
FPN [50]	1	38.9	56.4	14.9	14.2	2.2	13.2
PAN [51]	2	39.8	57.7	17.2	12.9	2.0	12.3
BiFPN-D0 [52]	6	37.5	55.0	11.2	18.2	3.1	8.6
BiFPN-D6	16	42.4	59.9	25.0	11.7	1.1	18.9
S-PAN [19]	2	43.4	60.3	21.0	12.0	1.7	26.4

in addressing local firing saturation. Removing MDS, despite slightly decreasing LFSI, significantly degrades performance due to the loss of residual learning capability.

To verify the derivation in Section IV-B1, we visualize the presynaptic input variance of EMS-ResNet and MDSNet in Fig. 9. In contrast to EMS-ResNet, our MDSNet maintains stable presynaptic input variance throughout the network. For EMS-ResNet, the presynaptic input to I-LIF#1 (i.e., the output of the previous residual block) exhibits gradually increasing variance, which is consistent with our theoretical analysis in Eq. 12.

2) *Ablations on the Depth of MDSNet*: In Section IV-C, we theoretically demonstrate that MDSNet overcomes gradient vanishing and exploding, enabling the training of deep networks. In this section, we further validate this through experiments. As shown in rows 5 and 8 to 10 of Table I, the feature extraction capability of MDSNet improves as the network depth increases. Notably, deeper networks exhibit lower LFSI and firing rates, suggesting that deeper architectures can effectively distribute neuronal activity across layers, mitigating local firing saturation issues.

3) *Ablations on Number of Fusion Directions in SMFM*: As shown in rows 1 to 4 of Table II, we compare the impact of different fusion direction numbers in SMFM. To ensure fair comparison, we adjust the network width to maintain comparable parameters across models. The results demonstrate that both LFSI and firing rate consistently decrease as the number of fusion directions increases. This validates our analysis in Section IV-D that more fusion directions help mitigate local firing saturation. However, detection performance begins to degrade beyond 4 directions, indicating that excessive structural complexity hinders optimization. Therefore, we adopt 4 fusion directions for SMFM.

We further investigate classical feature fusion modules from both ANN and SNN detectors [19], [50]–[52], adapting ANN methods for SNNs by replacing activations with I-LIF neurons. As shown in rows 5-9 of Table II, similar trends are observed. More fusion directions consistently lead to better suppression of local firing saturation. Notably, SMFM achieves the best detection performance while maintaining comparable power consumption and lower LFSI and firing rate.

4) *Ablations on SF-Block*: We replace the SF-Block in SMFM with the simplest single convolution to demonstrate its effectiveness. As shown in Table III, SF-Block significantly outperforms it in AP, LFSI, and firing rate, with only a

TABLE III
COMPARISON OF DIFFERENT FUSION BLOCKS. SF-BLOCK- AND SF-BLOCK+ REFER TO REMOVING ONE MS-BLOCK FROM SF-BLOCK AND ADDING AN ADDITIONAL MS-BLOCK, RESPECTIVELY.

Fusion Block	AP	AP ₅₀	Param (M)	Firing Rate(%)	LFSI (%)	Power (mJ)
7×7Conv	41.7	58.5	22.6	11.6	1.9	12.5
MS-Block	43.6	60.7	18.7	13.3	2.0	16.3
SF-Block-	43.8	60.9	20.3	12.0	1.6	17.8
SF-Block+	44.6	61.2	27.9	11.7	1.5	22.7
SF-Block	44.8	61.2	22.0	11.8	1.5	19.0

TABLE IV
IMPACT OF DIFFERENT TIME STEPS

Model	T×D	AP	AP ₅₀	Param (M)	Firing Rate(%)	LFSI (%)	Power (mJ)
SpikeYOLO	1×2	39.9	56.3	23.1	18.8	7.6	25.7
	1×4	43.9	60.4	23.1	12.2	1.7	33.0
	1×6	45.2	61.9	23.1	9.0	0.7	36.4
SpikeDet	1×2	41.2	56.8	22.0	18.1	6.7	15.7
	1×4	44.8	61.2	22.0	11.8	1.5	19.0
	1×6	45.6	62.3	22.0	8.8	0.5	20.9

slight increase in power consumption. Meanwhile, we conduct ablation on the two sub-blocks of SF-Block. Rows 2 and 3 in Table III retain only the MS-Block and the first sub-block, respectively, while row 4 extends the MS-Block to two instances. The results demonstrate that the proposed configuration effectively addresses the local firing saturation problem while achieving a better trade-off between performance and power consumption.

5) *Ablations on Time Step*: Given that SpikeDet provides more stable firing patterns and mitigates local firing saturation, it is expected to achieve comparable performance with fewer time steps. To demonstrate this, we conduct corresponding experiments. Since adjusting T is inefficient [19], we control the overall time steps by adjusting D instead. As shown in Table IV, compared to SpikeYOLO [19], our method achieves good performance even in low time steps. Moreover, performance gains remain modest as the time steps increase, demonstrating stronger robustness to variations in time steps.

D. Comparisons with State-of-The-Art Models

Based on the above ablation studies, we propose SpikeDet-S and SpikeDet-M using MDSNet34 and MDSNet104 as backbones, respectively. Furthermore, to explore the performance upper limit of SNN-based object detectors, we expand the width of SpikeDet-M to propose SpikeDet-L. We further increase T×D from 1×4 to 1×8, resulting in SpikeDet-X. The comparison results with state-of-the-art methods are shown in Table V. Compared to other SNN-based object detectors, our model achieves **52.2% AP** and **69.3% AP₅₀**, representing **+3.3%** and **+3.1%** improvements over the previous best (48.9% AP, 66.2% AP₅₀). Remarkably, this superior performance is achieved with only $\frac{1}{2}$ of the power consumption. This further strengthens the energy efficiency advantage of SNNs. Moreover, our method reduces LFSI by approximately 30% compared to SpikeYOLO at similar parameter scales, which further validates our analysis that local firing saturation constrains the advancement of SNNs in

TABLE V

PERFORMANCE COMPARISON WITH STATE-OF-THE-ART MODELS ON COCO 2017 VALIDATION DATASET. \dagger INDICATES RESULTS FROM MULTISCALE TESTING. SNNs INCLUDE FLOPs IN THE ENCODING LAYER. THEREFORE, IN THE COMPUTATIONAL COST COLUMN FOR SNNs, WE REPORT THE RESULTS IN THE FORMAT OF GFLOPS + GSOPS.

Method	Model	AP	AP ₅₀	AP ₇₅	AP _s	AP _m	AP _l	Param (M)	T × D	Firing Rate(%)	LFSI (%)	GFLOPs/GSOPS	Power (mJ)
ANNs	ATSS [21]	39.4	57.6	42.8	23.6	42.9	50.3	32.3	1	-	-	164.0	377.2
	DETR-DC5-R101 [33]	44.9	64.7	47.7	23.7	49.5	62.3	60.6	1	-	-	168.8	388.3
	RetinaNet \dagger [46]	41.8	62.9	45.7	25.6	45.1	54.1	56.7	1	-	-	330.2	759.5
	FCOS [20]	44.7	64.1	48.4	27.6	47.5	55.6	89.8	1	-	-	459.5	1056.8
	TOOD [53]	46.7	64.6	50.7	28.9	49.6	57.0	51.0	1	-	-	272.8	627.4
	CenterNet \dagger [47]	47.0	64.5	50.7	28.9	49.9	58.9	191.3	1	-	-	586.4	1348.8
	GCViTDet [54]	51.8	72.5	56.1	35.1	55.9	67.2	152.0	1	-	-	1014.9	2334.2
	Gold-YOLO-N [31]	39.6	55.7	-	19.7	44.1	57.0	5.6	1	-	-	12.1	27.6
	Gold-YOLO-S [31]	45.4	62.5	-	25.3	50.2	62.6	21.5	1	-	-	46.0	105.8
	Gold-YOLO-M [31]	49.8	67.0	-	32.3	55.3	66.3	41.3	1	-	-	87.5	197.8
	YOLOv8-N [30]	37.2	52.7	40.3	18.9	40.5	52.5	3.2	1	-	-	8.7	20.2
	YOLOv8-S [30]	43.9	60.8	47.6	25.3	48.7	59.5	11.2	1	-	-	28.6	66.2
	YOLOv8-M [30]	49.8	66.9	54.2	32.6	54.9	65.9	25.9	1	-	-	78.9	182.2
	RTMDet-T [48]	41.0	57.4	44.4	20.7	45.3	58.0	4.9	1	-	-	8.1	37.3
	RTMDet-S [48]	44.6	61.7	48.3	24.2	49.2	61.8	8.9	1	-	-	14.8	68.1
	RTMDet-M [48]	49.3	66.9	53.9	30.5	53.6	66.1	24.7	1	-	-	39.3	180.8
	YOLO-MS-XS [39]	42.8	60.0	46.7	23.1	46.8	60.1	5.1	1	-	-	17.4	40.0
	YOLO-MS-S [39]	45.4	62.8	49.5	25.9	49.6	62.4	8.7	1	-	-	30.0	69.0
	YOLO-MS [39]	49.7	67.2	54.0	32.8	53.8	65.6	23.3	1	-	-	77.6	178.5
	YOLOv11-N [32]	39.5	55.3	42.8	19.9	43.3	57.1	2.6	1	-	-	6.5	15.0
	YOLOv11-S [32]	47.0	63.9	50.6	29.9	51.6	64.4	9.4	1	-	-	21.5	49.5
	YOLOv11-M [32]	51.5	68.4	55.7	33.5	57.0	67.8	20.1	1	-	-	68.0	156.4
	YOLOv12-N [55]	40.6	56.7	43.8	20.2	45.2	58.2	2.6	1	-	-	6.5	15.0
	YOLOv12-S [55]	48.0	65.0	51.8	30.4	53.2	65.7	9.3	1	-	-	21.4	49.2
	YOLOv12-M [55]	52.5	69.6	57.1	35.9	58.2	68.8	20.2	1	-	-	67.5	155.3
SNNs	Spiking-YOLO [13]	25.7	-	-	-	-	-	10.2	3500	-	-	-	-
	EMS-YOLO [14]	30.1	50.1	-	-	-	-	33.9	4	24.9	11.4	1.9 + 27.3	29.0
	M-SpikeFormer [9]	-	50.3	-	-	-	-	75.0	1	-	-	5.0 + 143.6	140.8
	SUHD [17]	-	54.6	-	-	-	-	-	4	-	-	-	-
	E-SpikeFormer [10]	-	58.8	-	-	-	-	38.7	1 × 8	-	-	3.8 + 123.2	119.5
	MHSANet-YOLO [56]	-	66.9	-	-	-	-	76.3	1 × 8	-	-	-	49.2
	SpikeYOLO-N [19]	42.5	59.2	-	-	-	-	13.2	1 × 4	-	-	0.4 + 24.7	23.1
	SpikeYOLO-S [19]	45.5	62.3	49.2	25.5	50.4	61.3	23.1	1 × 4	12.8	2.2	0.5 + 37.2	34.6
	SpikeYOLO-S \dagger [19]	48.0	64.8	53.4	33.1	53.2	62.0	23.1	1 × 4	12.8	2.2	0.5 + 37.2	34.6
	SpikeYOLO-M [19]	47.4	64.6	-	-	-	-	48.1	1 × 4	-	-	0.6 + 74.6	68.5
	SpikeYOLO-L [19]	48.9	66.2	53.4	29.3	55.0	64.2	68.8	1 × 4	10.4	1.3	0.7 + 91.7	84.2
	SpikeYOLO-L \dagger [19]	51.2	68.0	56.7	36.4	56.7	65.6	68.8	1 × 4	10.4	1.3	0.7 + 91.7	84.2
	SpikeDet-S	46.2	62.6	50.5	26.8	51.2	60.8	22.0	1 × 4	12.3	1.7	1.0 + 19.3	19.6
	SpikeDet-S \dagger	48.2	65.3	53.6	32.4	53.2	62.2	22.0	1 × 4	12.3	1.7	1.0 + 19.3	19.6
	SpikeDet-M	48.0	64.8	52.1	27.5	54.1	63.6	48.2	1 × 4	9.6	1.1	1.0 + 24.8	24.6
	SpikeDet-M \dagger	50.2	67.5	55.5	34.1	55.9	64.3	48.2	1 × 4	9.6	1.1	1.0 + 24.8	24.6
	SpikeDet-L	49.6	66.5	54.3	29.6	55.5	65.0	75.2	1 × 4	8.8	1.0	1.2 + 34.0	33.4
	SpikeDet-L \dagger	51.4	68.6	56.9	36.6	56.8	65.4	75.2	1 × 4	8.8	1.0	1.2 + 34.0	33.4
	SpikeDet-X	50.9	67.6	54.7	31.3	57.1	66.5	75.2	1 × 8	4.3	0.2	1.2 + 41.7	40.4
	SpikeDet-X \dagger	52.2	69.3	57.2	36.9	57.2	65.9	75.2	1 × 8	4.3	0.2	1.2 + 41.7	40.4

performance and power consumption. Furthermore, compared to ANN-based methods, SpikeDet not only further narrows the gap between SNNs and ANNs, but also demonstrates a better trade-off between accuracy and power consumption. For example, SpikeDet-X achieves comparable accuracy to YOLOv12-M while providing **3.8 \times** the energy efficiency. The inference results of SpikeDet at various scales are presented in Fig. 10.

E. Evaluation on Object Detection Sub-Tasks

We further apply our proposed SpikeDet to four object detection sub-tasks, event camera on the GEN1 dataset [57], underwater on the URPC 2019 dataset [58], low-light on the ExDARK dataset [59], and dense scene on the CrowdHuman dataset [60]. These challenging scenarios allow us to evaluate the generalization capability and robustness of our method

across diverse conditions. Implementation details and dataset introductions are presented in Appendix B.

1) *Event Camera Object Detection*: As shown in Table VI, our method significantly outperforms both SNN-based and ANN-based object detectors on the GEN1 dataset. Importantly, this is achieved while maintaining the energy efficiency advantage of SNNs. This substantial improvement can be attributed to the unique characteristics of event-based data. The inherently sparse nature of event streams makes them already challenging to recognize, and local firing saturation further exacerbates this difficulty. Therefore, addressing local firing saturation is particularly crucial for event-based object detection. SpikeDet achieves LFSI values that are approximately 1.3 \times and 3.8 \times lower than those of SpikeYOLO and SFOD, respectively, demonstrating the effectiveness of our approach in mitigating this issue. Notably, when adjusting T × D from 5 × 1 to 4 × 2, performance improves despite an

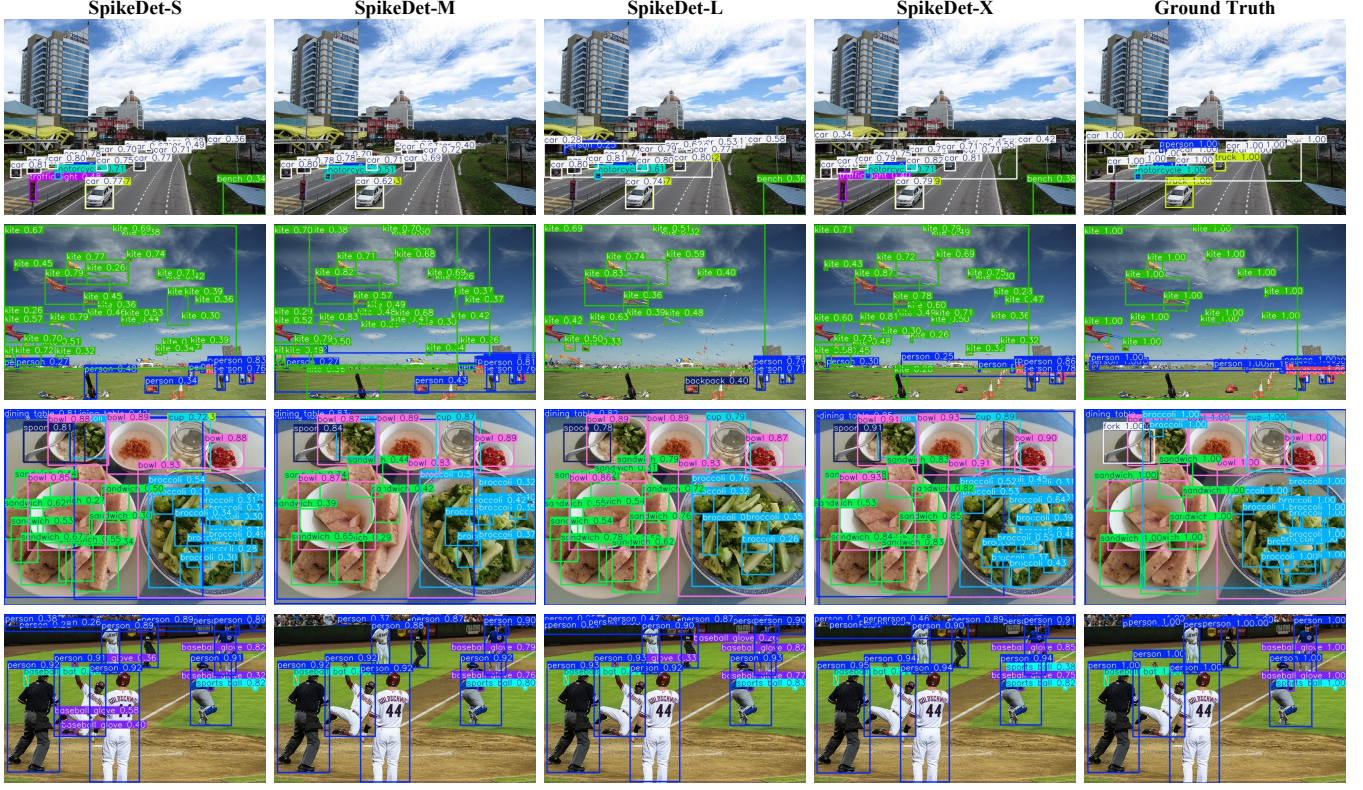


Fig. 10. **Detection results on the COCO 2017 dataset.** As the model scale increases, detection accuracy progressively improves.

TABLE VI
PERFORMANCE COMPARISON WITH STATE-OF-THE-ART MODELS ON
GEN1 DATASET. THE -RELU INDICATES THAT THE ACTIVATION
FUNCTION OF SPIKEDET-S IS CHANGED TO RELU, CONVERTING IT TO AN
ANN VERSION.

Model	AP	AP ₅₀	Param (M)	TxD	Firing Rate(%)	LFSI (%)	Power (mJ)
RED [61]	40.0	-	24.1	-	-	-	>24.1
SpikeDet-S-ReLU	46.2	66.5	22.0	1	-	-	45.2
ASTMNet [61]	46.7	-	>100	3	-	-	-
RVT [62]	47.2	-	18.5	10	-	-	116.7
S5-Vit-B [63]	47.4	-	18.2	10	-	-	-
VC-DenseNet [6]	18.9	-	24.3	5	37.2	-	5.8
Spiking-YOLO [13]	-	45.3	7.9	5	-	-	0.9
EMS-YOLO [14]	31.0	59.0	14.4	5	17.8	-	3.4
SFOD [16]	32.1	-	11.9	5	24.4	7.5	7.3
EAS-SNN [18]	37.5	69.9	25.3	5	20.3	-	28.1
SpikingVIT-B [15]	39.4	61.6	21.5	>64	18.0	-	-
SpikeYOLO-S [19]	38.9	66.4	23.1	5x1	10.5	1.3	19.7
SpikeYOLO-S [19]	40.4	67.2	23.1	4x2	14.0	2.5	12.9
SpikeDet-S	46.5	69.2	22.0	5x1	10.3	1.0	10.7
SpikeDet-S	47.6	70.1	22.0	4x2	13.7	2.0	9.9

increase in LFSI. This does not contradict our earlier analysis, as Fig. 8 compares models under similar TxD products (maintaining comparable temporal capacity). Under the same 4x2 configuration, SpikeDet maintains lower LFSI and superior performance compared to SpikeYOLO, confirming the effectiveness of our approach. Furthermore, to validate the importance of the SNN architecture, we replace I-LIF neurons with ReLU to implement an ANN version of SpikeDet. This causes significant performance degradation and increased

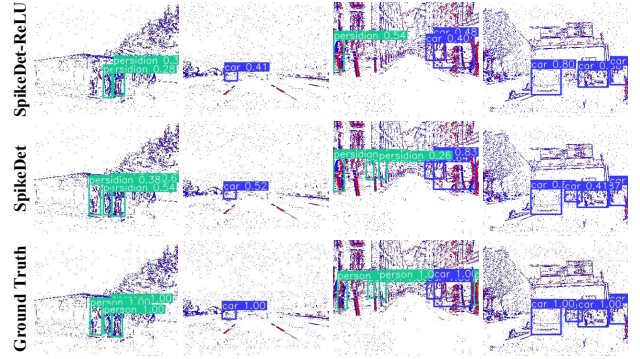


Fig. 11. **Detection results on the GEN1 dataset.**

power consumption, underscoring the effectiveness of SNNs for processing event data.

2) *Underwater Object Detection:* As shown in Table VII, on the URPC 2019 dataset, SpikeDet achieves significant improvements compared to other methods in both accuracy and power consumption. Specifically, compared to YOLOv9-S-UI, it achieves 1.4% AP improvement while reducing power consumption by 5.7 mJ. The superior performance of SpikeDet can be attributed to its more substantial LFSI reduction on URPC 2019 compared to other SNN-based methods. This is particularly beneficial for underwater scenarios where low-contrast and blurred objects demand enhanced feature discrim-

TABLE VII
PERFORMANCE COMPARISON WITH STATE-OF-THE-ART MODELS ON URPC 2019 DATASET. \dagger INDICATES RESULTS FROM MULTISCALE TESTING.

Model	AP	AP ₅₀	Param (M)	T × D	Firing Rate(%)	LFSI (%)	Power (mJ)
EfficientDet-D3 [52]	-	74.8	12.0	1	-	-	7.3
YOLOv8-N [30]	43.6	77.7	3.2	1	-	-	5.0
ULO [58]	-	65.1	3.8	1	-	-	3.0
YOLOv9-S-UI [64]	48.7	78.1	4.1	1	-	-	10.7
Spiking-YOLO [13]	22.4	53.7	8.7	3500	-	-	-
SU-YOLO [65]	42.9	78.8	7.0	4	-	-	3.0
SpikeYOLO-N [19]	46.9	83.1	14.2	1 × 4	12.5	1.3	5.8
SpikeYOLO-S [19]	47.9	83.8	23.1	1 × 4	12.2	1.2	8.6
SpikeDet-S	49.2	84.3	22.0	1 × 4	9.9	0.7	5.0
SpikeDet-S\dagger	50.1	86.1	22.0	1 × 4	9.9	0.7	5.0

TABLE VIII
PERFORMANCE COMPARISON WITH STATE-OF-THE-ART MODELS ON ExDARK DATASET. \dagger INDICATES RESULTS FROM MULTISCALE TESTING.

Model	AP	AP ₅₀	Param (M)	T × D	Firing Rate(%)	LFSI (%)	Power (mJ)
DETR-R50 [33]	25.0	55.0	41.3	1	-	-	219.0
YOLOv8-S [30]	40.7	66.2	11.1	1	-	-	65.6
SpikeYOLO-S [19]	40.4	65.1	23.1	1 × 4	12.0	1.1	36.1
SpikeDet-S	42.1	66.5	22.0	1 × 4	10.1	0.8	17.2
SpikeDet-S\dagger	43.0	69.6	22.0	1 × 4	10.1	0.8	17.2

ination for accurate detection.

3) *Low-Light Object Detection*: As shown in Table VIII, our method demonstrates robust performance under low-light conditions. By effectively mitigating local firing saturation, SpikeDet achieves a 2.6% AP improvement and 18.9 mJ power reduction compared to SpikeYOLO. Meanwhile, it also exhibits a better performance-power trade-off compared to ANN-based methods.

4) *Dense Scene Object Detection*: As shown in Table IX, SpikeDet achieves strong performance on the CrowdHuman dataset. It outperforms SpikeYOLO by 4.3% AP while consuming 19.2 mJ less power. In such crowded scenarios with heavy occlusions, the lower LFSI enables better discrimination of overlapping objects, contributing to improved detection accuracy.

VI. CONCLUSION

In this paper, we identify the local firing saturation problem in existing SNN-based object detection methods. This issue limits the achievement of better accuracy and energy efficiency. To address this, we propose SpikeDet, a novel SNN-based object detector. The key contribution is MDSNet, which effectively stabilizes synaptic input distribution and mitigates local firing saturation through the proposed MDS and architectural improvements. For feature fusion, we propose SMFM, which employs a multi-directional fusion strategy to enhance multi-scale detection while preserving neuron firing patterns. Additionally, we introduce the Local Firing Saturation Index (LFSI) to quantify the effectiveness of our approach in addressing local firing saturation. Experimental results demonstrate that our model outperforms other SNN-based models in accuracy on the COCO 2017 dataset. Moreover, it achieves superior performance on diverse downstream tasks,

TABLE IX
PERFORMANCE COMPARISON WITH STATE-OF-THE-ART MODELS ON CrowdHuman DATASET. \dagger INDICATES RESULTS FROM MULTISCALE TESTING.

Model	AP	AP ₅₀	Param (M)	T × D	Firing Rate(%)	LFSI (%)	Power (mJ)
DETR-R50 [33]	27.8	55.5	41.3	1	-	-	219.0
YOLOv8-S [30]	51.7	79.3	11.1	1	-	-	65.3
SpikeYOLO-S [19]	50.4	78.7	23.1	1 × 4	11.2	1.0	37.6
SpikeDet-S	52.8	78.8	22.0	1 × 4	10.1	0.7	18.4
SpikeDet-S\dagger	54.7	80.4	22.0	1 × 4	10.1	0.7	18.4

including event-based GEN1, underwater URPC 2019, low-light ExDARK, and dense scene CrowdHuman, demonstrating strong generalization capability. Meanwhile, it maintains significantly lower power consumption, achieving an optimal balance between detection accuracy and energy efficiency.

REFERENCES

- [1] Z. Huang, J. Ding, Z. Pan, H. Li, Y. Fang, Z. Yu, and J. K. Liu, “Converting high-performance and low-latency snns through explicit modeling of residual error in anns,” *IEEE Trans. Neural Netw. Learn. Syst.*, vol. 36, no. 9, pp. 16 788–16 802, 2025.
- [2] W. Maass, “Networks of spiking neurons: The third generation of neural network models,” *Neural Netw.*, vol. 10, no. 9, pp. 1659–1671, 1997.
- [3] R. Zhang, L. Leng, K. Che, H. Zhang, J. Cheng, Q. Guo, J. Liao, and R. Cheng, “Accurate and efficient event-based semantic segmentation using adaptive spiking encoder-decoder network,” *IEEE Trans. Neural Netw. Learn. Syst.*, vol. 36, no. 5, pp. 9326–9340, 2025.
- [4] N. Skatchkovsky, O. Simeone, and H. Jang, “Learning to time-decode in spiking neural networks through the information bottleneck,” in *Proc. Adv. Neural Inf. Process. Syst.*, Dec. 2021, pp. 17 049–17 059.
- [5] C. Cao, X. Fu, Y. Zhu, Z. Sun, and Z.-J. Zha, “Event-driven video restoration with spiking-convolutional architecture,” *IEEE Trans. Neural Netw. Learn. Syst.*, vol. 36, no. 1, pp. 866–880, 2025.
- [6] L. Cordone, B. Miramond, and P. Thierion, “Object detection with spiking neural networks on automotive event data,” in *Proc. Int. Joint Conf. Neural Netw. (IJCNN)*, 2022, pp. 1–8.
- [7] S. Barchid, J. Mennesson, J. Eshraghian, C. Djébara, and M. Benamoun, “Spiking neural networks for frame-based and event-based single object localization,” *Neurocomputing*, vol. 559, Nov. 2023, art. no. 126805.
- [8] A. Safa, F. Corradi, L. Keuninckx, I. Ocket, A. Bourdoux, F. Catthoor, and G. G. Gielen, “Improving the accuracy of spiking neural networks for radar gesture recognition through preprocessing,” *IEEE Trans. Neural Netw. Learn. Syst.*, vol. 34, no. 6, pp. 2869–2881, 2021.
- [9] M. Yao, J. Hu, T. Hu, Y. Xu, Z. Zhou, Y. Tian, B. Xu, and G. Li, “Spike-driven transformer v2: Meta spiking neural network architecture inspiring the design of next-generation neuromorphic chips,” in *Proc. Int. Conf. Learn. Represent.*, May 2024, pp. 1–23.
- [10] M. Yao, X. Qiu, T. Hu, J. Hu, Y. Chou, K. Tian, J. Liao, L. Leng, B. Xu, and G. Li, “Scaling spike-driven transformer with efficient spike firing approximation training,” *IEEE Trans. Pattern Anal. Mach. Intell.*, vol. 47, no. 4, pp. 2973–2990, Jan. 2025.
- [11] S. Liu, D. Huang, and Y. Wang, “Pay attention to them: Deep reinforcement learning-based cascade object detection,” *IEEE Trans. Neural Netw. Learn. Syst.*, vol. 31, no. 7, pp. 2544–2556, 2019.
- [12] Q. Zhou, H. Shi, W. Xiang, B. Kang, and L. J. Latecki, “Dpnet: Dual-path network for real-time object detection with lightweight attention,” *IEEE Trans. Neural Netw. Learn. Syst.*, vol. 36, no. 3, pp. 4504–4518, 2024.
- [13] S. Kim, S. Park, B. Na, and S. Yoon, “Spiking-yolo: Spiking neural network for energy-efficient object detection,” in *Proc. AAAI Conf. Artif. Intell.*, vol. 34, Apr. 2020, pp. 11 270–11 277.
- [14] Q. Su, Y. Chou, Y. Hu, J. Li, S. Mei, Z. Zhang, and G. Li, “Deep directly-trained spiking neural networks for object detection,” in *Proc. IEEE/CVF Int. Conf. Comput. Vis. (ICCV)*, Oct. 2023, pp. 6555–6565.
- [15] L. Yu, H. Chen, Z. Wang, S. Zhan, J. Shao, Q. Liu, and S. Xu, “Spikingvit: A multiscale spiking vision transformer model for event-based object detection,” *IEEE Trans. Cogn. Develop. Syst.*, vol. 17, no. 1, pp. 130–146, Jul. 2024.

[16] Y. Fan, W. Zhang, C. Liu, M. Li, and W. Lu, "Sfod: Spiking fusion object detector," in *Proc. IEEE/CVF Conf. Comput. Vis. Pattern Recognit. (CVPR)*, Jun. 2024, pp. 17 191–17 200.

[17] J. Qu, Z. Gao, T. Zhang, Y. Lu, H. Tang, and H. Qiao, "Spiking neural network for ultralow-latency and high-accurate object detection," *IEEE Trans. Neural Netw. Learn. Syst.*, vol. 36, no. 3, pp. 4934–4946, Mar. 2024.

[18] Z. Wang, Z. Wang, H. Li, L. Qin, R. Jiang, D. Ma, and H. Tang, "Eas-sn: End-to-end adaptive sampling and representation for event-based detection with recurrent spiking neural networks," in *Proc. Eur. Conf. Comput. Vis. (ECCV)*, Sep. 2024, pp. 310–328.

[19] X. Luo, M. Yao, Y. Chou, B. Xu, and G. Li, "Integer-valued training and spike-driven inference spiking neural network for high-performance and energy-efficient object detection," in *Proc. Eur. Conf. Comput. Vis. (ECCV)*, Sep. 2024, pp. 253–272.

[20] Z. Tian, C. Shen, H. Chen, and T. He, "Fcos: Fully convolutional one-stage object detection," in *Proc. IEEE/CVF Int. Conf. Comput. Vis. (ICCV)*, Oct. 2019, pp. 9627–9636.

[21] S. Zhang, C. Chi, Y. Yao, Z. Lei, and S. Z. Li, "Bridging the gap between anchor-based and anchor-free detection via adaptive training sample selection," in *Proc. IEEE/CVF Conf. Comput. Vis. Pattern Recognit. (CVPR)*, Jun. 2020, pp. 9759–9768.

[22] Y. Hu, L. Deng, Y. Wu, M. Yao, and G. Li, "Advancing spiking neural networks toward deep residual learning," *IEEE Trans. Neural Netw. Learn. Syst.*, vol. 36, no. 2, pp. 2353–2367, Feb. 2024.

[23] T.-Y. Lin, M. Maire, S. Belongie, J. Hays, P. Perona, D. Ramanan, P. Dollár, and C. L. Zitnick, "Microsoft coco: Common objects in context," in *Proc. Eur. Conf. Comput. Vis. (ECCV)*, vol. 8693, 2014, pp. 740–755.

[24] H. Zheng, Y. Wu, L. Deng, Y. Hu, and G. Li, "Going deeper with directly-trained larger spiking neural networks," in *Proc. AAAI Conf. Artif. Intell.*, vol. 35, Feb. 2021, pp. 11 062–11 070.

[25] W. Fang, Z. Yu, Y. Chen, T. Huang, T. Masquelier, and Y. Tian, "Deep residual learning in spiking neural networks," *Proc. Adv. Neural Inf. Process. Syst.*, vol. 34, pp. 21 056–21 069, Dec. 2021.

[26] P. Viola and M. Jones, "Rapid object detection using a boosted cascade of simple features," in *Proc. IEEE/CVF Conf. Comput. Vis. Pattern Recognit. (CVPR)*, vol. 1, Dec. 2001, pp. I–I.

[27] J. Yin, T. Chen, G. Pei, H. Liu, Y. Yao, L. Nie, and X. Hua, "Semi-supervised semantic segmentation with multi-constraint consistency learning," *IEEE Trans. Multimedia*, vol. 27, pp. 6449–6461, 2025.

[28] J. Yin, Y. Chen, Z. Zheng, J. Zhou, and Y. Gu, "Uncertainty-participation context consistency learning for semi-supervised semantic segmentation," in *Proc. IEEE Int. Conf. Acoust., Speech, Signal Process. (ICASSP)*. IEEE, Apr. 2025, pp. 1–5.

[29] B. Li, C. Liu, M. Shi, X. Chen, X. Ji, and Q. Ye, "Proposal distribution calibration for few-shot object detection," *IEEE Trans. Neural Netw. Learn. Syst.*, vol. 36, no. 1, pp. 1911–1918, 2025.

[30] G. Jocher, A. Chaurasia, and J. Qiu, "Ultralytics yolov8," 2023. [Online]. Available: <https://github.com/ultralytics/ultralytics>

[31] C. Wang, W. He, Y. Nie, J. Guo, C. Liu, Y. Wang, and K. Han, "Gold-yolo: Efficient object detector via gather-and-distribute mechanism," *Proc. Adv. Neural Inf. Process. Syst.*, vol. 36, pp. 51 094–51 112, Dec. 2023.

[32] G. Jocher and J. Qiu, "Ultralytics yolov11," 2024. [Online]. Available: <https://github.com/ultralytics/ultralytics>

[33] N. Carion, F. Massa, G. Synnaeve, N. Usunier, A. Kirillov, and S. Zagoruyko, "End-to-end object detection with transformers," in *Proc. Eur. Conf. Comput. Vis. (ECCV)*, Aug. 2020, vol. 12346, pp. 213–229.

[34] S. Kim, S. Park, B. Na, J. Kim, and S. Yoon, "Towards fast and accurate object detection in bio-inspired spiking neural networks through bayesian optimization," *IEEE Access*, vol. 9, pp. 2633–2643, Nov. 2020.

[35] A. L. Hodgkin and A. F. Huxley, "A quantitative description of membrane current and its application to conduction and excitation in nerve," *J. Physiol.*, vol. 117, no. 4, p. 500, 1952.

[36] W. Gerstner, W. M. Kistler, R. Naud, and L. Paninski, *Neuronal dynamics: From single neurons to networks and models of cognition*. Cambridge University Press, 2014.

[37] L. F. Abbott, "Lapicque's introduction of the integrate-and-fire model neuron (1907)," *Brain Res. Bull.*, vol. 50, no. 5–6, pp. 303–304, 1999.

[38] Y. Zhao, W. Lv, S. Xu, J. Wei, G. Wang, Q. Dang, Y. Liu, and J. Chen, "Detsr beat yolos on real-time object detection," in *Proc. IEEE/CVF Conf. Comput. Vis. Pattern Recognit. (CVPR)*, Jun. 2024, pp. 16 965–16 974.

[39] Y. Chen, X. Yuan, J. Wang, R. Wu, X. Li, Q. Hou, and M.-M. Cheng, "Yolo-ms: Rethinking multi-scale representation learning for real-time object detection," *IEEE Trans. Pattern Anal. Mach. Intell.*, vol. 47, no. 6, pp. 4240–4252, Feb. 2025.

[40] Y. Kim, H. Park, A. Moitra, A. Bhattacharjee, Y. Venkatesha, and P. Panda, "Rate coding or direct coding: Which one is better for accurate, robust, and energy-efficient spiking neural networks?" in *Proc. IEEE Int. Conf. Acoustics, Speech, Signal Process.*, May 2022, pp. 71–75.

[41] K. He, X. Zhang, S. Ren, and J. Sun, "Delving deep into rectifiers: Surpassing human-level performance on imagenet classification," in *Proc. IEEE/CVF Int. Conf. Comput. Vis. (ICCV)*, Dec. 2015, pp. 1026–1034.

[42] Z. Chen, L. Deng, B. Wang, G. Li, and Y. Xie, "A comprehensive and modularized statistical framework for gradient norm equality in deep neural networks," *IEEE Trans. Pattern Anal. Mach. Intell.*, vol. 44, no. 1, pp. 13–31, Jul. 2020.

[43] B. Poole, S. Lahiri, M. Raghu, J. Sohl-Dickstein, and S. Ganguli, "Exponential expressivity in deep neural networks through transient chaos," *Proc. Adv. Neural Inf. Process. Syst.*, vol. 29, Dec. 2016.

[44] Z. Zheng, P. Wang, W. Liu, J. Li, R. Ye, and D. Ren, "Distance-iou loss: Faster and better learning for bounding box regression," in *Proc. AAAI Conf. Artif. Intell.*, vol. 34, Apr. 2020, pp. 12 993–13 000.

[45] X. Li, W. Wang, L. Wu, S. Chen, X. Hu, J. Li, J. Tang, and J. Yang, "Generalized focal loss: Learning qualified and distributed bounding boxes for dense object detection," in *Proc. Adv. Neural Inf. Process. Syst.*, vol. 33, Dec. 2020, pp. 21 002–21 012.

[46] T.-Y. Lin, P. Goyal, R. Girshick, K. He, and P. Dollár, "Focal loss for dense object detection," in *Proc. IEEE/CVF Int. Conf. Comput. Vis. (ICCV)*, Oct. 2017, pp. 2980–2988.

[47] K. Duan, S. Bai, L. Xie, H. Qi, Q. Huang, and Q. Tian, "Centernet++ for object detection," *IEEE Trans. Pattern Anal. Mach. Intell.*, vol. 46, no. 5, pp. 3509–3521, Dec. 2023.

[48] C. Lyu, W. Zhang, H. Huang, Y. Zhou, Y. Wang, Y. Liu, S. Zhang, and K. Chen, "Rtdet: An empirical study of designing real-time object detectors," 2022, arXiv:2212.07784.

[49] H. Zhang, M. Cisse, Y. N. Dauphin, and D. Lopez-Paz, "Mixup: Beyond empirical risk minimization," 2018, arXiv:1710.09412.

[50] T.-Y. Lin, P. Dollár, R. Girshick, K. He, B. Hariharan, and S. Belongie, "Feature pyramid networks for object detection," in *Proc. IEEE/CVF Conf. Comput. Vis. Pattern Recognit. (CVPR)*, Jul. 2017, pp. 2117–2125.

[51] S. Liu, L. Qi, H. Qin, J. Shi, and J. Jia, "Path aggregation network for instance segmentation," in *Proc. IEEE/CVF Conf. Comput. Vis. Pattern Recognit. (CVPR)*, Jun. 2018, pp. 8759–8768.

[52] M. Tan, R. Pang, and Q. V. Le, "Efficientdet: Scalable and efficient object detection," in *Proc. IEEE/CVF Conf. Comput. Vis. Pattern Recognit. (CVPR)*, Jun. 2020, pp. 10 781–10 790.

[53] C. Feng, Y. Zhong, Y. Gao, M. R. Scott, and W. Huang, "Tood: Task-aligned one-stage object detection," in *Proc. IEEE/CVF Int. Conf. Comput. Vis. (ICCV)*, Oct. 2021, pp. 3490–3499.

[54] Y. Quan, D. Zhang, and J. Tang, "Generalized concordant vision transformer with masked image tokens for object detection," *IEEE Trans. Circuits Syst. Video Technol.*, vol. 35, no. 11, pp. 10 616–10 631, 2025.

[55] Y. Tian, Q. Ye, and D. Doermann, "Yolov12: Attention-centric real-time object detectors," 2025, arXiv:2502.12524.

[56] L. Fan, H. Shen, X. Lian, Y. Li, M. Yao, G. Li, and D. Hu, "A multisympatic spiking neuron for simultaneously encoding spatiotemporal dynamics," *Nature Commun.*, vol. 16, no. 1, 2025, Art. no. 7155.

[57] P. de Tournemire, D. Nitti, E. Perot, D. Migliore, and A. Sironi, "A large scale event-based detection dataset for automotive," 2020, arXiv:2001.08499.

[58] L. Wang, X. Ye, S. Wang, and P. Li, "Ulo: An underwater light-weight object detector for edge computing," *Machines*, vol. 10, no. 8, Jul. 2022, Art. no. 629.

[59] Y. P. Loh and C. S. Chan, "Getting to know low-light images with the exclusively dark dataset," *Comput. Vis. Image Underst.*, vol. 178, pp. 30–42, 2019.

[60] S. Shao, Z. Zhao, B. Li, T. Xiao, G. Yu, X. Zhang, and J. Sun, "Crowdhuman: A benchmark for detecting human in a crowd," 2018, arXiv:1805.00123.

[61] E. Perot, P. De Tournemire, D. Nitti, J. Masci, and A. Sironi, "Learning to detect objects with a 1 megapixel event camera," *Proc. Adv. Neural Inf. Process. Syst.*, vol. 33, pp. 16 639–16 652, Dec. 2020.

[62] M. Gehrig and D. Scaramuzza, "Recurrent vision transformers for object detection with event cameras," in *Proc. IEEE/CVF Conf. Comput. Vis. Pattern Recognit. (CVPR)*, Jun. 2023, pp. 13 884–13 893.

[63] N. Zubic, M. Gehrig, and D. Scaramuzza, "State space models for event cameras," in *Proc. IEEE/CVF Conf. Comput. Vis. Pattern Recognit. (CVPR)*, Jun. 2024, pp. 5819–5828.

- [64] W. Pan, J. Chen, B. Lv, and L. Peng, "Optimization and application of improved yolov9s-ui for underwater object detection," *Appl. Sci.*, vol. 14, no. 16, Aug. 2024, Art. no. 7162.
- [65] C. Li, W. Liu, G. Gong, X. Ding, and X. Zhong, "Su-yolo: Spiking neural network for efficient underwater object detection," *Neurocomputing*, vol. 644, Sep. 2025, art. no. 130310.
- [66] X. Glorot and Y. Bengio, "Understanding the difficulty of training deep feedforward neural networks," in *Proc. Int. Conf. Artif. Intell. Stat. (AISTATS)*. JMLR Workshop and Conference Proceedings, 2010, pp. 249–256.
- [67] M. Taki, "Deep residual networks and weight initialization," 2017, arXiv:1709.02956.

APPENDIX A PROOF OF THE PROPOSITIONS

A. Proof of Proposition 1

Proposition 1. For d stacked LCB layers ($d \geq 1$) with arbitrary kernel sizes, under the convolution zero-mean weight and zero bias initialization, the output at the $(n+d)$ -th layer $\mathbf{y}^{t,n+d}$ is uncorrelated with the input at the n -th layer $\mathbf{x}^{t,n}$.

We first analyze the case of a single LCB, conducting our analysis according to the processing sequence of its internal components. The first component is the I-LIF neuron. It receives input $\mathbf{x}^{t,n}$ and produces output spikes $\mathbf{o}^{t,n} = \text{Clip}(\text{round}(\mathbf{u}^{t,n}), 0, D)$.

Subsequently, we combine the convolution with tBN following [24], where the merged weight and bias are:

$$W'_{m,n} = \lambda_n \frac{\alpha V_{th} W_{m,n}}{\sqrt{\sigma_{inf,n}^2 + \epsilon}}, \quad (22)$$

$$B'_{m,n} = \lambda_n \frac{\alpha V_{th} (B_{m,n} - \mu_{inf,n})}{\sqrt{\sigma_{inf,n}^2 + \epsilon}} + \beta_n. \quad (23)$$

Here W represents the weight and B represents the bias, with subscripts m, n respectively indicating the mapping from the m -th feature map of the previous layer to the n -th feature map of the next layer, where the superscript $'$ indicates the transformed version. For the parameters in tBN, λ_n and β_n are learnable parameters, α is a hyperparameter, and $\sigma_{inf,n}^2$ and $\mu_{inf,n}$ are the expectations of $E[\mathbf{x}^{t,n}]$ and $\text{Var}[\mathbf{x}^{t,n}]$ over the entire dataset.

Taking the expectation of the merged weight:

$$E[W'_{m,n}] = \lambda_n \frac{\alpha V_{th}}{\sqrt{\sigma_{inf,n}^2 + \epsilon}} E[W_{m,n}]. \quad (24)$$

Since $E[W_{m,n}] = 0$ (zero-mean weight initialization) and $\lambda_n, \alpha, V_{th}, \sigma_{inf,n}^2, \epsilon$ are deterministic constants:

$$E[W'_{m,n}] = 0. \quad (25)$$

Thus, tBN merging preserves the zero-mean property of weights. Furthermore, given that $B_{m,n}$ is initialized to zero, and according to the default parameters in [24], $\mu_{inf,n}$ and β_n are also 0, so from Eq. 23, we get $B'_{m,n} = 0$.

As in [41], [66], [67], we assume that the elements in $\mathbf{x}^{t,n}$ and $W_{m,n}$ are independent and identically distributed (i.i.d.). For rigorous covariance analysis, we consider individual tensor elements. Let $y_i^{t,n}$, $x_i^{t,n}$, $w_j^{t,n}$, $b_i^{t,n}$, and $o_j^{t,n}$ denote arbitrary elements of $\mathbf{y}^{t,n}$, $\mathbf{x}^{t,n}$, $W'_{m,n}$, $B'_{m,n}$, and $\mathbf{o}^{t,n}$, respectively.

The $\mathbf{y}^{t,n}$ represents the output of a single LCB, and its element y_i can be expressed as

$$y_i^{t,n} = \sum_{j \in \text{RF}(i)} w_j^{t,n} \cdot o_j^{t,n} + b_i^{t,n}, \quad (26)$$

where $\text{RF}(i)$ denotes the receptive field corresponding to output position i . For simplicity,

$$y_i^{t,n} = \sum_j w_j^{t,n} \cdot o_j^{t,n} + b_i^{t,n}. \quad (27)$$

From the above derivation, we can obtain $b_i^{t,n} = 0$, therefore,

$$y_i^{t,n} = \sum_j w_j^{t,n} \cdot o_j^{t,n}. \quad (28)$$

Then, we derive the covariance between the output $y_i^{t,n}$ and the input $x_i^{t,n}$,

$$\text{Cov}(y_i^{t,n}, x_i^{t,n}) = E[y_i^{t,n} \cdot x_i^{t,n}] - E[y_i^{t,n}]E[x_i^{t,n}]. \quad (29)$$

Since $E[x_i^{t,n}] = 0$,

$$\text{Cov}(y_i^{t,n}, x_i^{t,n}) = E[y_i^{t,n} \cdot x_i^{t,n}]. \quad (30)$$

Expanding the above equation, we get

$$E[y_i^{t,n} \cdot x_i^{t,n}] = E \left[\left(\sum_j w_j^{t,n} \cdot o_j^{t,n} \right) \cdot x_i^{t,n} \right]. \quad (31)$$

Exchanging summation and expectation,

$$E[y_i^{t,n} \cdot x_i^{t,n}] = \sum_j E[w_j^{t,n} \cdot o_j^{t,n} \cdot x_i^{t,n}]. \quad (32)$$

Since weights $w_j^{t,n}$ are independent of inputs at initialization,

$$E[w_j^{t,n} \cdot o_j^{t,n} \cdot x_i^{t,n}] = E[w_j^{t,n}] \cdot E[o_j^{t,n} \cdot x_i^{t,n}]. \quad (33)$$

Therefore:

$$E[w_j^{t,n} \cdot o_j^{t,n} \cdot x_i^{t,n}] = 0 \cdot E[o_j^{t,n} \cdot x_i^{t,n}] = 0. \quad (34)$$

This holds for all j . From Eq. 32:

$$E[y_i^{t,n} \cdot x_i^{t,n}] = \sum_j E[w_j^{t,n} \cdot o_j^{t,n} \cdot x_i^{t,n}] = \sum_j 0 = 0. \quad (35)$$

$$\text{Cov}(y_i^{t,n}, x_i^{t,n}) = 0. \quad (36)$$

Therefore, for a single LCB, its output \mathbf{y} is uncorrelated with the input \mathbf{x} .

Finally, we consider d stacked LCBs ($d \geq 1$) and analyze them using mathematical induction. Assume that for $(d-1)$ stacked LCBs, we have $\text{Cov}(y^{t,n+d-1}, x^{t,n}) = 0$. We prove that this also holds for d stacked LCBs, i.e., $\text{Cov}(y^{t,n+d}, x^{t,n}) = 0$.

The output of layer $(n+d)$ is:

$$y_i^{t,n+d} = \sum_j w_j^{t,n+d} \cdot o_j^{t,n+d}. \quad (37)$$

Since $E[\mathbf{x}^{t,n}] = 0$,

$$\begin{aligned} \text{Cov}(y_i^{t,n+d}, x_i^{t,n}) &= E[y_i^{t,n+d} \cdot x_i^{t,n}] \\ &= \sum_j E[w_j^{t,n+d} \cdot o_j^{t,n+d} \cdot x_i^{t,n}]. \end{aligned} \quad (38)$$

At initialization, weights $w_j^{t,n+d}$ are independent of the input $\mathbf{x}^{t,n}$ at layer n . Although $o_j^{t,n+d}$ depends on $\mathbf{x}^{t,n}$ through intermediate layers, the weight independence holds:

$$E[w_j^{t,n+d} \cdot o_j^{t,n+d} \cdot x_i^{t,n}] = E[w_j^{t,n+d}] \cdot E[o_j^{t,n+d} \cdot x_i^{t,n}]. \quad (39)$$

Since $E[w_j^{t,n+d}] = 0$ by zero-mean initialization,

$$E[w_j^{t,n+d} \cdot o_j^{t,n+d} \cdot x_i^{t,n}] = 0. \quad (40)$$

Thus $\text{Cov}(y_i^{t,n+d}, x_i^{t,n}) = 0$. By mathematical induction, $\text{Cov}(\mathbf{y}^{t,n+d}, \mathbf{x}^{t,n}) = 0$ for any starting layer n and d stacked LCB layers. This completes the proof of Proposition 2.

B. Proof of Proposition 2

Proposition 2. *For I-LIF neurons, the variance of the membrane potential is proportional to the variance of the input, i.e., $\text{Var}[\mathbf{u}^{t,n}] \propto \text{Var}[\mathbf{x}^{t,n}]$.*

From Eqs. 1 and 3 in the main paper, we obtain:

$$\begin{aligned} \mathbf{u}^{t,n} &= \tau(\mathbf{u}^{t-1,n} - \mathbf{o}^{t-1,n}) + \mathbf{x}^{t,n-1} \\ &= \tau[\tau(\mathbf{u}^{t-2,n} - \mathbf{o}^{t-2,n}) + \mathbf{x}^{t-1,n-1} - \mathbf{o}^{t-1,n}] + \mathbf{x}^{t,n-1} \\ &= \tau^t \mathbf{u}^{0,n} - \sum_{p=1}^{t-1} \tau^{t-p} \mathbf{o}^{p,n} + \sum_{p=1}^t \tau^{t-p} \mathbf{x}^{p,n-1}. \end{aligned} \quad (41)$$

Since I-LIF can fire integer-valued spikes, each spike emission reduces the membrane potential to a level close to 0. Therefore, we can assume that the last spike is fired at time step t' , and thus ignore the influence of \mathbf{o} on the membrane potential, yielding:

$$\mathbf{u}^{t,n} = \tau^t \mathbf{u}^{0,n} + \sum_{p=t'}^t \tau^{t-p} \mathbf{x}^{p,n-1}. \quad (42)$$

Moreover, since τ is a tiny constant, which is only 0.25 in our implementation, the above equation can be simplified to:

$$\mathbf{u}^{t,n} = \mathbf{x}^{t,n-1} + \tau \mathbf{x}^{t-1,n-1}. \quad (43)$$

Assume that \mathbf{x} is independently and identically distributed for each time step t . Thus, we can conclude that the membrane potential variance is proportional to the input variance, i.e., $\text{Var}[\mathbf{u}^{t,n}] \propto \text{Var}[\mathbf{x}^{t,n-1}]$.

C. Proof of Proposition 3

Proposition 3. *For MDSNet, when the encoding layer output follows $\mathbf{x}^t \sim \mathcal{N}(0, 1)$ and each block output follows $\mathbf{x}^{t,j} \sim \mathcal{N}(0, 1)$, the network satisfies: $\phi(\mathbf{J}\mathbf{J}^T) \approx 1$.*

Theorem 2. (Theorem 4.2. in [42]) *Given $\mathbf{J} := \sum_j \mathbf{J}_j$, where \mathbf{J}_j is a series of independent random matrices. If at most one matrix in \mathbf{J}_j is not a central matrix, we have*

$$\phi(\mathbf{J}\mathbf{J}^T) = \sum_j \phi(\mathbf{J}_j\mathbf{J}_j^T). \quad (44)$$

We first analyze each MDS-Block, which consists of two distinct pathways: the residual path and the shortcut path. Consequently, we designate their respective Jacobian matrices as \mathbf{J}_{res} and \mathbf{J}_{sc} .

For the residual path, since all its components satisfy Definition 2 for MDS-Block1 and MDS-Block2 [14], [24], [42], we can derive:

$$\alpha_2^{l,\text{res}} = \phi(\mathbf{J}_{\text{res}}\mathbf{J}_{\text{res}}^T)\alpha_2^{l-1}, \quad (45)$$

$$\phi(\mathbf{J}_{\text{res}}\mathbf{J}_{\text{res}}^T) = \frac{\alpha_2^{l,\text{res}}}{\alpha_2^{l-1}}. \quad (46)$$

The same applies to the shortcut path, therefore:

$$\phi(\mathbf{J}_{\text{sc}}\mathbf{J}_{\text{sc}}^T) = \frac{\alpha_2^{l,\text{sc}}}{\alpha_2^{l-1}}. \quad (47)$$

Based on Theorem 2, we can derive for MDS-Block1 and MDS-Block2:

$$\phi(\mathbf{J}_{\text{MDS-Block}}\mathbf{J}_{\text{MDS-Block}}^T) = \frac{\alpha_2^{l,\text{res}} + \alpha_2^{l,\text{sc}}}{\alpha_2^{l-1}}. \quad (48)$$

Therefore, if the encoding layer output follows $\mathbf{x}^t \sim \mathcal{N}(0, 1)$ and each block output follows $\mathbf{x}^{t,j} \sim \mathcal{N}(0, 1)$, we can derive:

$$\phi(\mathbf{J}_{\text{MDS-Block}}\mathbf{J}_{\text{MDS-Block}}^T) = 1. \quad (49)$$

Thus, for the entire MDSNet, according to the above equation and the derivation from Theorem 1, we can derive:

$$\phi(\mathbf{J}\mathbf{J}^T) \approx 1. \quad (50)$$

APPENDIX B MORE EXPERIMENTAL SETUP

1) Datasets Introduction: The GEN1 dataset [57] represents the initial large-scale collection for object detection using event cameras. It comprises car footage spanning over 39 hours, captured by the GEN1 device with a spatial resolution of 304×240 . The dataset includes bounding box annotations for vehicles and pedestrians, provided at rates of 1 to 4Hz. These labels accumulate to a total exceeding 255,000 across the recordings.

The URPC 2019 dataset [58] is designed for the 2019 Underwater Robot Picking Contest and comprises 4,707 annotated underwater images across four marine object categories: scallops, starfish, echinus, and holothurian. The dataset splits include 3,767 training images, 695 validation images, and 245 test images.

The ExDARK dataset [59] is designed for low-light object detection, featuring 7,363 images captured under various illumination conditions ranging from extremely dark environments to twilight scenarios. The dataset encompasses 12 object categories: Bicycle, Boat, Bottle, Bus, Car, Cat, Chair, Cup, Dog, Motorbike, People, and Table, with bounding box annotations provided for all instances. In this study, we split the dataset into training, validation, and test sets with a ratio of 6:2:2.

The CrowdHuman dataset [60] focuses on human detection in densely populated scenarios. It comprises approximately 470K annotated human instances across its training and validation sets, with an average density of 22.6 individuals per image and substantial occlusion variations. Annotations include bounding boxes for the head, visible body region, and complete body for each person. The dataset provides

TABLE X

THE STRUCTURE OF MDSNET FOR COCO 2017. THE OUTPUT SIZE COLUMN SPECIFIES THE SPATIAL RESOLUTION AND CHANNEL COUNT OF FEATURE MAPS PRODUCED AT EACH STAGE. THE NUMBERS IN PARENTHESES INDICATE THE NUMBER OF MS-BLOCKS CONTAINED IN THE RESIDUAL PATH OF THE MDS-BLOCK.

Stage	Output Size	MDSNet10	MDSNet18	MDSNet34	MDSNet104
Encoding	320×320, 64	Encoding Block			
Conv1	160×160, 64	MS2Block2(0)	MS2Block2(1)	MS2Block2(2)	MS2Block2(2)
Conv2	80×80, 128	MS2Block2(0)	MS2Block2(1)	MS2Block2(1) MS2Block1(1)	MS2Block2(3) MS2Block1(3)
Conv2	40×40, 256	MS2Block2(0)	MS2Block2(1)	MS2Block2(2) MS2Block1(2)	MS2Block2(15) MS2Block1(15)
Conv4	20×20, 512	MS2Block2(0)	MS2Block2(1)	MS2Block2(2)	MS2Block2(3) MS2Block1(3)
Conv5	20×20, 512	SpikeSPPF			

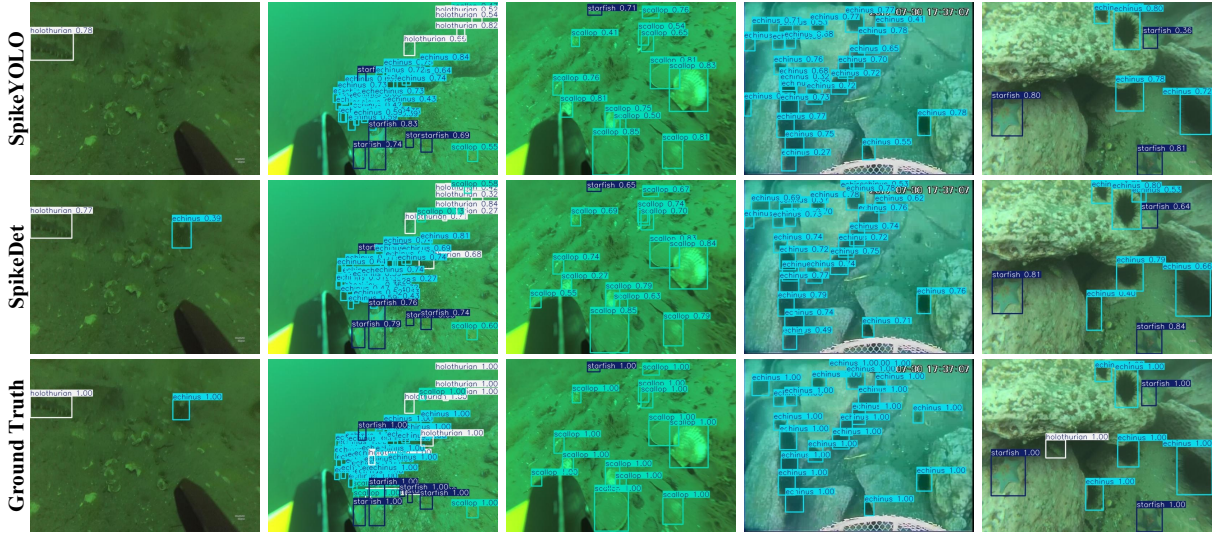


Fig. 12. Detection result on the URPC 2019 dataset.

15,000 training images, 4,370 validation images, and 5,000 test images, featuring comprehensive annotations across diverse scenarios.

2) *More Implementation Details:* The MDSNet structure is detailed in Table X. For SpikeDet-L, we increase the channel dimensions of MDSNet104 by a factor of 1.25 to improve model performance. On the Gen1 dataset, we employ the zoom-in and zoom-out augmentation strategies from [62]. The model is trained for 100 epochs with a batch size of 64. For URPC 2019, ExDARK, and CrowdHuman datasets, we employ mosaic augmentation. Specifically, following [58], [64], [65], we resize images to 320×320 for URPC 2019, while using 640×640 for the other datasets. All models are trained for 300 epochs with a batch size of 64.

datasets, as shown in Figs. 12, 13, and 14. These results demonstrate that our model achieves excellent performance on the object detection subtasks.

APPENDIX C MORE VISUALIZATION

In this section, we present the visualization results of our model on the URPC 2019, ExDARK, and CrowdHuman

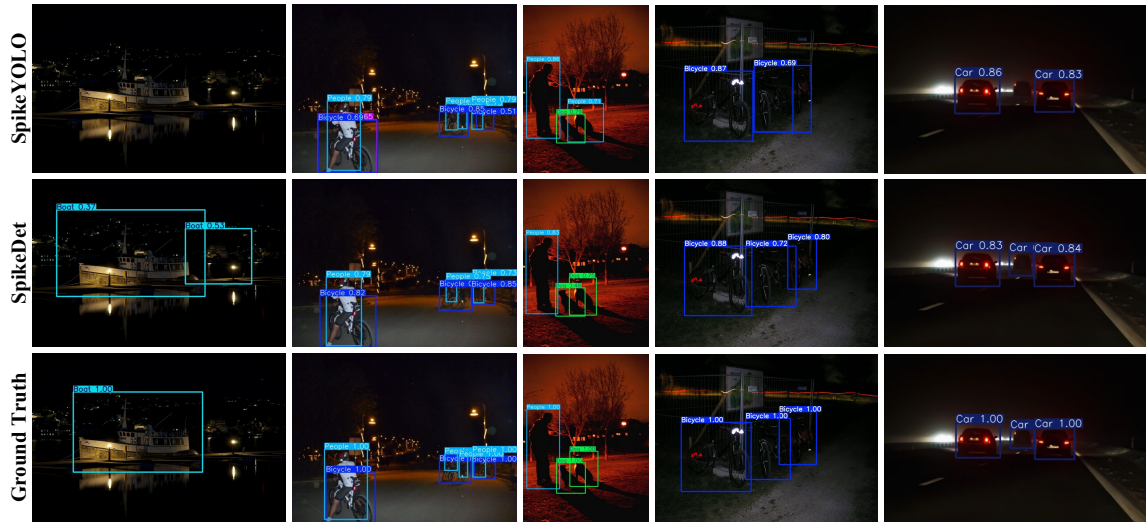


Fig. 13. Detection result on the ExDARK dataset.



Fig. 14. Detection result on the CrowdHuman dataset.